Climatology of the CO vertical distribution on Mars based on ACS TGO measurements

Anna A. Fedorova, Alexander V. Trokhimovskiy, Franck Lefèvre, Kevin Olsen, Oleg I. Korablev, Franck Montmessin, Nikolay I. Ignatiev, Alexander Lomakin, François Forget, Denis A. Belyaev, et al.

Climatology of the CO vertical distribution on Mars based on ACS TGO measurements

Anna Fedorova[1], Alexander Trokhimovskiy[1], Franck Lefèvre[2], Kevin S. Olsen[3], Oleg Korablev[1], Franck Montmessin[2], Nikolay Ignatiev[1], Alexander Lomakin[1], Francois Forget[4], Denis Belyaev[1], Juan Alday[3,5], Mikhail Luginin[1], Michael Smith[6], Andrey Patrakeev[1], Alexey Shakun[1] & Alexey Grigoriev[1,7]

[1]Space Research Institute (IKI) RAS, Moscow, Russian Federation.

[2]LATMOS, CNRS, Sorbonne Université, Université Versailles Saint-Quentin-en-Yvelines , Guyancourt, France.

[3]Department of Physics, University of Oxford, Oxford, UK.

[4]Laboratoire de Météorologie Dynamique, Sorbonne Université, Centre National de la Recherche Scientifique, Jussieu, Paris, France

[5]School of Physical Sciences, The Open University, Milton Keynes, UK

[6]NASA Goddard Space Flight Center, Greenbelt, USA

[7]Australian National University, Research School of Astronomy and Astrophysics, Mount Stromlo Observatory, Advanced Instrumentation and Technology Centre, Canberra, Australia

Corresponding author: Anna Fedorova (fedorova@iki.rssi.ru).

Key points:

- The first climatology of CO vertical profiles is collected for the period Ls=163° of Martian Year 34 to the end of Martian Year 35.
- The mean CO volume mixing ratio is ~960 ppmv at 0–35 km and 45°S–45°N

- Strong enrichment of CO, >3000 ppmv, is detected at 10-20 km at Ls=100-200 in high southern latitudes and above 50 km at equinoxes near Poles.

Abstract

Carbon monoxide is a non-condensable gas in the Martian atmosphere produced by the photolysis of CO_2. Its abundance responds to the condensation and sublimation of CO_2 from the polar caps, resulting in seasonal variations of the CO mixing ratio. ACS onboard the ExoMars Trace Gas Orbiter have measured CO in infrared bands by solar occultation. Here we provide the first long-term monitoring of the CO vertical distribution at the altitude range from 0 to 80 km for 1.5 Martian years from Ls=163° of MY34 to the end of MY35. We obtained a mean CO mixing ratio of ~960 ppmv at latitudes from 45°S to 45°N and altitudes below 40 km, mostly consistent with previous observations. We found a strong enrichment of CO near the surface at Ls=100-200° in high southern latitudes with a layer of 3000-4000 ppmv, corresponding to local depletion of CO_2. At equinoxes we found an increase of the CO mixing ratio above 50 km to 3000–4000 ppmv at high latitudes of both hemispheres explained by the downwelling flux of the Hadley circulation on Mars, which drags the CO enriched air. General circulation models tend to overestimate the intensity of this process, bringing too much CO. The observed minimum of CO in the high and mid-latitudes southern summer atmosphere amounts to 700-750 ppmv, agreeing with nadir measurements. During the global dust storm of MY34, when the H_2O abundance peaks, we see less CO than during the calm MY35, suggesting an impact of HO_x chemistry on the CO abundance.

Plain language summary

Carbon monoxide (CO) is a product of the photodissociation of the main component of the Martian atmosphere, CO_2 (96%). During the polar night on Mars, the temperature drops so low that ~30% of the global atmospheric carbon dioxide freezes out, condensed into snowflakes. They settle to the ground to form a seasonal polar cap, which sublimates in spring. Unlike CO_2,

CO is not a condensable species, so its relative abundance increases when CO_2 and the atmospheric pressure drops, forming a prominent seasonal cycle. This behavior of CO was well documented by spacecraft measurements of column abundances, while its vertical distribution remained poorly known until recently. Still, it helps to separate the impacts of atmospheric dynamics and chemistry, addressing the problem of the Martian atmosphere's stability. We present the first climatology of the CO vertical distribution lasting more than one Martian year based on solar occultations by the ExoMars Trace Gas Orbiter. We report a previously unobserved CO layer near the surface in high southern latitudes in late winter and spring and document the difference between two Martian years caused by the global dust storm. These observations give new challenges to General Circulation Models for understanding the modern atmosphere of Mars.

1. Introduction

Carbon monoxide (CO) is produced by the photolysis of CO_2 and plays a crucial role in the photochemical cycle that stabilizes the atmosphere's composition. CO was discovered by Kaplan et al. (1969). Its observed abundance is by two orders of magnitude lower than the expected abundance of ~8% in the context of a dry atmosphere (Nair et al., 1994). This inconsistency posed a problem for the stability of CO_2 in the Martian atmosphere, later resolved by introducing catalytic reactions with the H_2O photolysis products (like OH) (McElroy and Donahue (1972); Parkinson and Hunten (1972)). Still, a problem persists in quantitative understanding of the HO_x chemistry because current models mostly underestimate the amount of CO on Mars (Lefèvre & Krasnopolsky, 2017).

The CO abundance on Mars has been measured by high-resolution ground-based spectroscopy from infrared lines located in the 3-0 (1.57 μm, Krasnopolsky, 2003; Krasnopolsky, 2007), 2-0 (2.3 μm, Krasnopolsky, 2015; Billebaud et al., 1998) and 1-0 (4.7 μm, Billebaud et al., 1992) bands of CO and rotational microwave spectrum (Clancy et al., 1990*;* Lellouch et al., 1991). The column-averaged CO mixing ratios inferred from these observations represented

mostly the abundance in the lower atmosphere. It varied from 600±150 ppmv (parts per million by volume) to 800±200 ppmv. Krasnopolsky et al. (2003) first reported the north-south asymmetry of the CO distribution at Ls=112° with CO volume mixing ratios (VMRs) varying from 830 ppmv in the northern middle latitudes to 1250 ppmv at 50°S. The first map of seasonal-latitudinal variations of CO based on several latitudinal tracks (Krasnopolsky 2007) showed an increase of CO abundance up to 1600 ppmv at Ls=112-173°.

The seasonal distribution of CO was observed in nadir observations made with OMEGA (Observatoire pour la Minéralogie, l'Eau, les Glaces et l'Activité) and PFS (Planetary Fourier Spectrometer) onboard Mars Express (Encrenaz et al., 2006; Billebaud et al., 2009; Sindoni et al., 2011; Bouche et al., 2019; 2021), CRISM (Compact Reconnaissance Imaging Spectrometer for Mars) on board the Mars Reconnaissance Orbiter (Smith et al., 2009, 2018) and recently NOMAD (Nadir and Occultation for Mars Discovery) onboard the ExoMars Trace Gas Orbiter (TGO) (Smith et al., 2021) using the 2.3 μm (2-0) and 4.7 μm (1-0) absorption bands. These observations have shown strong seasonal variations of CO, especially in high latitudes. The minimal values (down to 200 ppmv based on CRISM) have been found in the southern summer high latitudes. At low-to-mid latitudes, the CO_2 condensation-sublimation cycle leads to a broad peak (~1000-1100 ppmv) around the northern autumnal equinox at about Ls = 180° (evident in global climate models (GMCs), CRISM and PFS data, less so in NOMAD). This maximum is a result of the transport of the CO enriched air from the winter polar region. CO behaves as other non-condensable gases like N_2, Ar, O_2, expected to vary in response to the condensation-sublimation cycle of CO_2 into and from the seasonal polar caps. Seasonal variations of argon were measured by Mars Odyssey gamma-ray spectrometer (Sprague et al., 2004; 2012); similarly, variations of Ar, N_2, O_2 and CO were found at the surface by Sample Analysis at Mars (SAM) onboard the Curiosity rover (Trainer et al., 2019). This phenomenon is well reproduced by GCM simulations (Forget et al., 2008; Smith et al., 2018; Holmes et al., 2019).

The annual mean value of CO remains a topic of debate. Nadir measurements from PFS, CRISM and NOMAD support a global average of ~800 ppmv (Bouche et al., 2021, Smith et al., 2018, 2021). Earth-based observations yielded a lower value of ~700 ppmv (Krasnopolsky 2015). In situ measurements by SAM/Curiosity resulted in an even lower value of 580 ppmv (Trainer et al., 2019). After several Martian years of observations, such small mixing ratios were never confirmed from orbit at the MSL location (Smith et al., 2018, 2021).

While the global seasonal trends of the CO column are relatively well understood, its vertical distribution was poorly documented before the arrival of TGO at Mars. Using PFS, Bouche et al. (2019; 2021) retrieved CO vertical profiles by exploiting the vertical sensitivity of the 4.7 μm band. These measurements carry information mainly on the CO column below 15 km with enhanced sensitivity near the surface. However, their inferred vertical gradients at 0–20 km can not be reproduced by 3D climate models, which rely on our current understanding of Martian photochemistry (Forget et al., 2008). The authors concluded that their observed vertical gradients are artificial and caused by the vertical sensitivity of PFS.

In 2018, the ExoMars TGO began its science phase by observing Mars' atmosphere from its orbit. Two scientific instruments onboard TGO, the Atmospheric Chemistry Suite (ACS) (Korablev et al., 2018) and NOMAD (Vandaele et al., 2018), can sound the vertical structure of the atmosphere in solar occultation mode. ACS includes three high-resolution infrared spectrometers: NIR (near-infrared), MIR (middle infrared) and TIRVIM (thermal infrared) (Korablev et al., 2018). All three channels measure the vertical distribution of CO in three spectroscopic bands used previously in ground-based and spacecraft observations: 1.57 μm (NIR), 2.3 μm (MIR and TIRVIM) and 4.7 μm (TIRVIM). The first CO vertical profiles were inferred from ACS MIR at altitudes 20–120 km and Ls=164–220° before and during the global dust storm (GDS) of Mars year (MY) 34. They showed a prominent depletion in the CO mixing ratio up to 100 km, pointing to the importance of CO oxidation during wetter GDS conditions (Olsen et al., 2021).

Here, we report the first long-term observations of the CO vertical distribution on Mars. They are based primarily on the ACS NIR dataset and compared to ACS MIR and TIRVIM solar occultations. We study the seasonal and latitudinal variations of the CO profiles for MY 34 and 35, focusing on the interannual variability, and compare our data with the Laboratoire de Météorologie Dynamique (LMD) GCM results, including photochemistry (Lefèvre et al., 2004, 2021).

2. Measurements and the CO retrievals

2.1 Dataset

ACS is a dedicated solar occultation experiment, with all three channels operating in this mode. In solar occultation, the transmittance at different altitudes in the atmosphere is derived by taking the ratio of each spectrum with the reference solar spectrum obtained when observing the Sun outside the atmosphere (before or after an occultation sequence). This method provides high sensitivity since the airmass factor at the limb is ten times greater than in nadir, and the Sun is the brightest input source of the Solar system. The polar and circular orbit of the spacecraft (78° of inclination, 2 hours period and 400 km above the surface of the planet) was optimized to provide vertical profiling at unprecedented spatial and temporal resolution (up to 24 occultations per day). A misalignment between ACS MIR and NOMAD lines-of-sight (LOS) does not allow simultaneous measurements of all occultation experiments onboard TGO. Thus, the number of occultations had to be divided between NOMAD and ACS. However, the field-of-view (FOV) of NIR and TIRVIM allow measurements with NOMAD pointing that result in different coverage and fullness of datasets for these two ACS spectrometers.

The densest dataset, which constitutes the basis of this study, was produced by ACS NIR, which provides CO measurements in the 1.57 μm band at 0-60 km for each occultation. From the beginning of the TGO science phase in April 2018 (Ls=163° of MY 34) to January 2021 (Ls=360° of MY 35), ACS NIR collected about 6050 profiles (Figure 1). ACS NIR can use two

kinds of pointing (ACS-driven and NOMAD-driven), and we have analyzed all available occultation profiles (the NOMAD pointing results in ~40% of profiles).

ACS MIR gives access to a much stronger band of CO located at 2.35 μm, resulting in the capability to measure CO up to 90–110 km. The MIR dataset includes 620 occultations performed using secondary grating position 6 (see section 2.3). The validity of the NIR and MIR profiles was established by comparing the two sets of profiles.

ACS TIRVIM measures both the 2.35 μm band and the strongest fundamental 4.7 μm band (see fig. S6). The interferogram can be obtained at high- or low-resolution observation mode defined by the maximum optical path difference (MOPD). The MOPD of the TIRVIM interferometer can be as large as 5 cm^{-1}. In the high-resolution mode (MOPD = 4.3 cm), the spectral sampling $\Delta\nu$and the spectral resolution (full-width at half-maximum (FWHM) of the instrumental function with Hamming apodization) are equal to 0.11 and 0.21 cm^{-1}, respectively. In the low-resolution mode MOPD = 0.97 cm, $\Delta\nu$ = 0.51 cm^{-1} and FWHM = 0.94 cm^{-1}. The largest number of occultations was done in the low-resolution mode, while only 20 orbits were done in high resolution mode, but with worse signal-to-noise ratio (SNR). For the analysis, we used the low-resolution TIRVIM observations of the 4.7 μm band to validate NIR and MIR results at 0–40 km. TIRVIM ceased operations in December 2019 (Ls=115°, MY 35) after having recorded ~1000 solar occultations since the beginning of the mission.

The following sections describe the datasets and the processing of ACS MIR, TIRVIM and NIR, and introduce the validation of the retrieved CO profiles. An in-depth comparison of CO VMRs retrieved from different channels can be found in Supplementary Material.

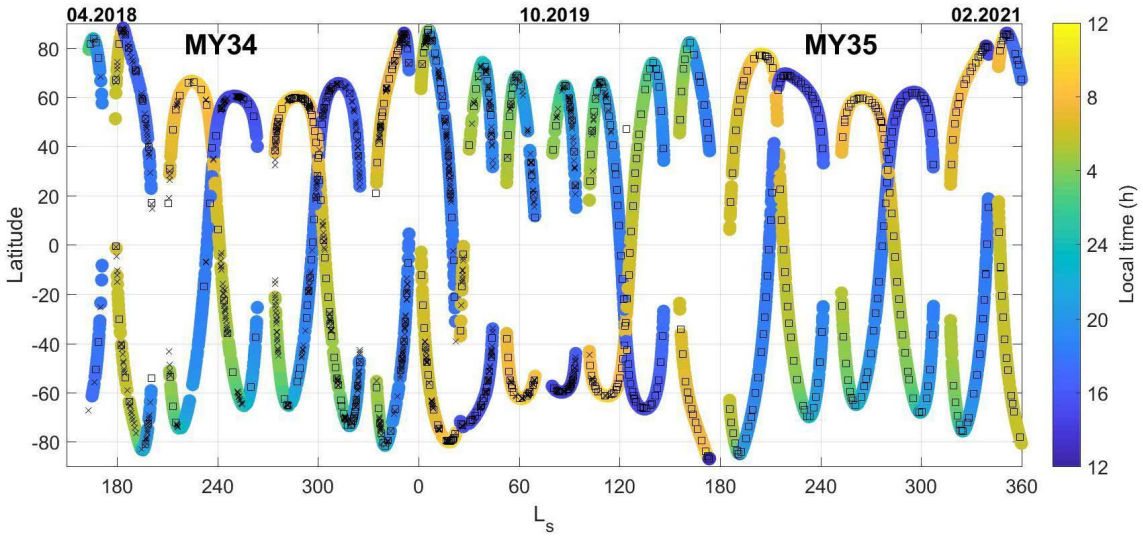

Figure 1. Observational coverage of ACS solar occultations. The color circles, where colours indicate the local time of the occultation, show NIR observations. Black squares show MIR observations of CO, and black crosses show TIRVIM observations.

2.2 NIR

ACS NIR combines an acousto-optical tunable filter (AOTF), used as a monochromator that can be commanded to isolate a specific wavelength bandpass whose width corresponds to the free spectral range of the echelle grating that operates at high diffraction orders. It covers the 0.7–1.7 μm spectral range using diffraction orders 101 through 49 (Trokhimovskiy et al., 2015a; Korablev et al., 2018). During an occultation, ACS NIR measures ten pre-selected diffraction orders every 2 s, including the absorption bands of H_2O and CO_2. The resolving power of the spectrometer is varied from 20000 to 28000 depending on spectral range and pixel position over the detectors (Korablev et al., 2018).

The instantaneous FOV in the direction perpendicular to the limb is small (~0.02°) and limited by the slit width. The FOV corresponds to an instantaneous vertical resolution of 500–600 m at the tangent altitude of the line of sight. The time to measure one diffraction order is 0.2 s. The effective vertical resolution depends on the β-angle (the angle between the orbit plane and the direction to the Sun). It is generally better than 1 km for each diffraction order. Horizontal

resolution (along the slit) is 1.5–5 km and is determined by the number of stacked detector lines. The number of detector lines measured in a single occultation and position of the lines on the detector depends on the pointing direction (NOMAD and ACS MIR-driven) and the available downlink volume. It varies from 6 to 30 lines; the solar image size on the detector limits the upper boundary. Averaging 30 detector lines does not worsen vertical resolution since that dimension of FOV is oriented along the limb. The SNR for an individual pixel and pure solar signal in the AOTF maximum equals about ~600 for the MIR pointing and ~300 for the NOMAD pointing. We averaged 6–25 lines with the maximal signal, excluding the solar image edges, resulting in an SNR of 800–3000, depending on the occultation.

The calibration of ACS NIR spectrometer included the detection of dead and hot pixels, AOTF function characterizations (important for order overlapping), AOTF frequency-wavelength calibrations and the drift of AOTF calibrations with temperature, blaze function characterization, spectral calibrations (pixel wavelength) and instrumental line shape (ILS) determining the spectral power (Korablev et al., 2018). During this work on the calibrated NIR transmission data, the wavelength drift is additionally corrected using positions of gaseous absorption lines.

The high spectral resolution and the SNR of NIR allow to resolve very weak absorption bands as well as rotational structure of abundant gases like CO_2. This makes NIR a sensitive instrument for temperature retrieval in the atmosphere. Diffraction order 49 of NIR (6318–6387 cm^{-1}) was initially used to retrieve the temperature and CO_2 density using the 1.57 μm CO_2 band (Fedorova et al., 2020). This order also contains a weaker overlapping CO band. Even if hardly noticeable within the strong CO_2 band, the retrieval algorithm detects the CO lines well thanks to their periodic structure. It permits measuring the CO mixing ratio from 0 to 60-70 km. Figure 2 shows examples of spectra fitted in order 49 with and without CO. The 1.57 μm band was already used for measuring CO abundance in the Martian atmosphere using high-resolution ground-based observations (Krasnopolsky, 2003).

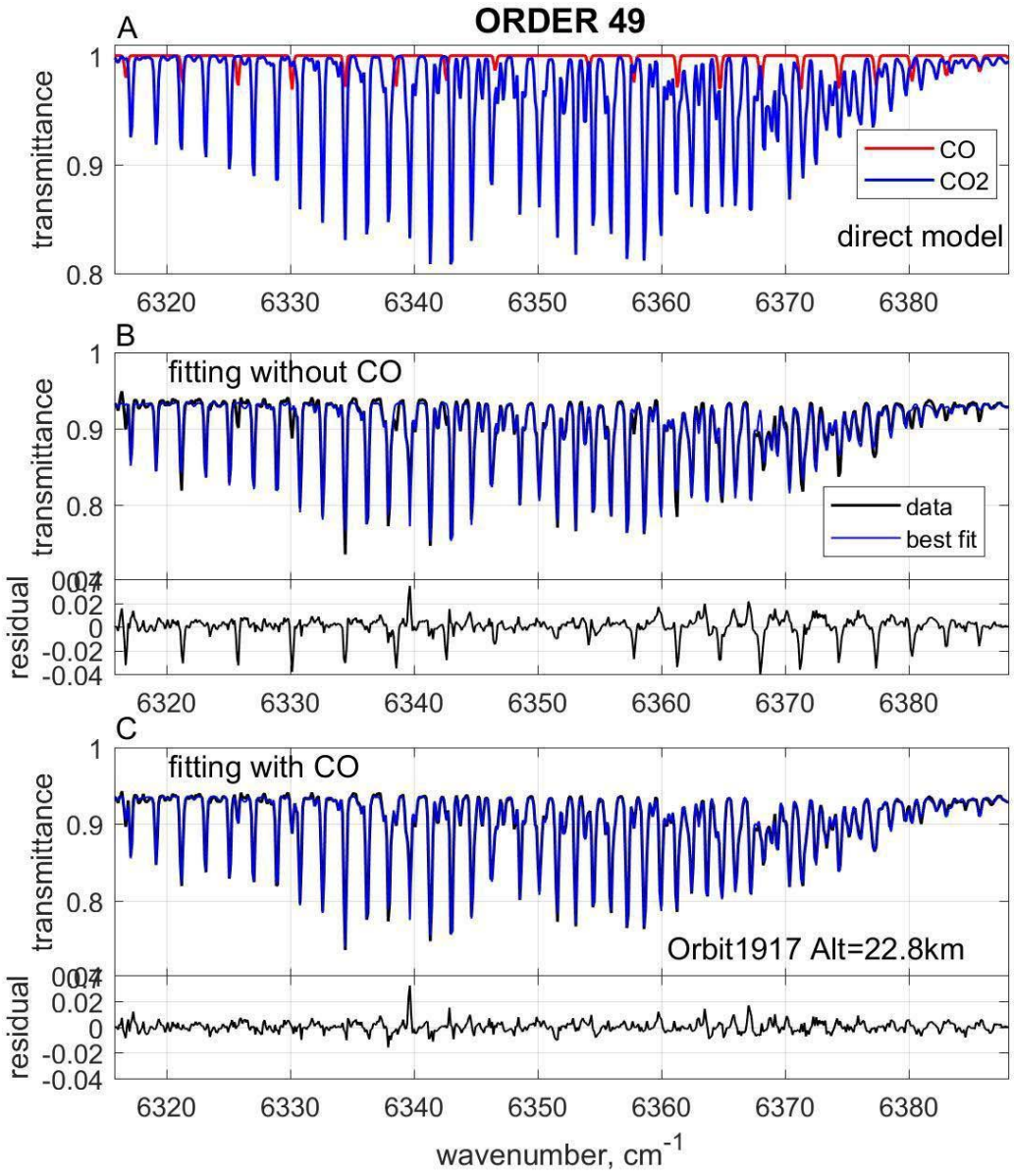

Figure 2. Example of ACS NIR spectrum measured in order 49 at 23 km altitude showing the benefit of fitting with a model including both CO_2 and CO. A): a synthetic model of CO_2 (blue) and CO (red, 1000 ppmv) absorption bands. B): spectrum observed (in black) at orbit 1917, Ls=167°, the latitude of 82°, east longitude of –92.3° and local time 21:15 with its best fit (in blue) without CO and fit residual; (C) the same observed spectrum with its best fit (in blue) with CO and fit residual.

The forward transmission model is computed for a corresponding number of atmospheric layers (40 to 130 depending on orbit) using a pre-computed look-up table of absorption cross-

sections (as a function of pressure and temperature) calculated line-by-line. The spectral line parameters for the CO_2 and CO are taken from the HITRAN 2016 database (Gordon et al., 2017) with CO_2-broadening coefficients for CO (Li et al., 2015) and self-broadening for CO_2. The order overlapping (two close orders from both sides) due to distant side lobes of the AOTF function was taken into account additionally in the direct model before the comparison with the measured spectrum is made.

The retrieval algorithm is based on a Levenberg–Marquardt iterative scheme and Tikhonov regularization to smooth the profile and minimize the uncertainties (Ceccherini, 2005). As an initial assumption, the temperature and pressure from the Mars Climate Database (MCD) v. 5.3 (climatology) profiles have been used (Millour et al., 2019). The initial mixing ratio of CO was assumed to be 1000 ppm at all altitudes.

The inverse problem is divided into two steps. The first step includes fitting for temperature, pressure and CO mixing ratio independently, based on the resolved rotational structure of the CO_2 band. The retrieval algorithm returns all the unknowns at all altitudes at the same time, i.e. the vertical profiles (see Fedorova et al., 2018; 2020 for details). We do not fit the CO_2 volume mixing ratio, as its vmr is supposed to be constant up to 100 km. However, in polar regions, the CO_2 vmr is predicted by GCMs to decrease above 80 km but this region is higher than the NIR sensitivity to the CO lines and didn't impact on the NIR CO retrievals. Once the solution is obtained, Tikhonov regularization is applied, customary for vertical inversions to smooth the profile and minimize the errors. The obtained smoothed profiles serve as an initial assumption for the following iteration with Levenberg–Marquardt. The algorithm converges within 3-6 iterations independently of initial assumptions as shown in Fedorova et al. (2020), and demonstrates a good sensitivity of the Jacobian to the temperature profile thanks to the pronounced CO_2 rotational structure in our spectral range.

However, the retrieval of the vertical profiles of pressure with the rotational structure of the CO_2 band generates sometimes unrealistic results. In ~30% of profiles of the analyzed dataset, we observed a bend, a drop of the pressure curve at some altitudes, in contradiction with the hydrostatic law (Fedorova et al., 2020). Therefore, in the second step, we assume that the atmospheric layers are in hydrostatic equilibrium to constrain the retrieval of temperature and pressure simultaneously. We define a pressure P_0 at an altitude level z_0 where the uncertainties on the previous step are minimal (the highest data quality), and then compute the pressure profile from the hydrostatic equilibrium, integrating the retrieved T profile above and below the P_0 level:

$$P(h) = P_o \, exp(-\int_{z0}^{h} \frac{g(z)M(z)}{T(z)k} dz), \quad (261)$$

where z is the altitude, $g(z)$ is the acceleration due to gravity, $M(z)$ is the molecular weight (taken from the MCD), k is the Boltzmann constant, h is the height at which P is being determined. Once the pressure is calculated, we repeat the temperature retrieval with only two free parameters, temperature and CO vmr, and perform several iterations until the pressure and temperature profiles converge. At first, the uncertainty on the retrieved quantities is given by the covariance matrix of the solution. In the second step, the uncertainty of P_0 is also taken into account. The more detailed retrieval algorithm and comparison of results is described in (Fedorova et al., 2020). The retrieval products from order 49 are the pressure, atmospheric temperature and CO mixing ratio, as shown in figure 5.

The solar occultation is a self-calibrated method and instrumental uncertainties are minimized when dividing a spectrum observed through the atmosphere to the pure solar spectrum. In case of NIR, the retrieval of CO mixing ratio, temperature and pressure from the same order also minimize the instrumental uncertainties. Nonetheless, the main uncertainty of the calibration and data processing which can be critical for the CO retrieval is an order overlapping. It is coming from distant side lobes of the AOTF function which was calibrated in

laboratory and in flight (Korablev et al., 2018). We estimate that the width of the AOTF function in order 49 and the contribution of side lobes can make the uncertainties up to 5% to the retrieval of the CO mixing ratio (see fig. S1). The other important contribution is the atmospheric temperature profile used for the retrieval. The accuracy of temperature profiles retrieved from order 49 was discussed in Fedorova et al. (2020) and is sensitive to the AOTF calibration and initial assumptions. It was also estimated from the cross-calibration of the ACS NIR and ACS-MIR retrievals of position 4 (2.7 μm CO_2 band) (see Belyaev et al., 2021; Alday et al., 2021) where the data of two experiments were consistent inside 5-7 K below 70-80 km and the MIR data were mostly warmer. The line strength of strong CO lines inside order 49 is sensitive to temperature with averaged +0.3% per -1 Kelvin. It means if the atmospheric temperature is 7 K colder, we underestimate the CO mixing ratio by ~ 2%. Finally, the total systematic uncertainties of the NIR retrieval does not exceed 7%.

2.3 MIR

The ACS MIR (mid-infrared) channel is a crossed-dispersion echelle spectrometer dedicated to solar occultation measurements in the 2.3–4.5 μm range with spectral resolving power of ~30,000. The channel can only sample a fraction (~160 cm^{-1}) of the full range on a single observation. To access a particular interval, a secondary dispersion grating is rotated to one of 11 positions (Korablev et al., 2018; Trokhimovskiy et al., 2015b, 2020). During an occultation, MIR is operated in one pre-chosen secondary grating position. Spectra are recorded on a two-dimensional detector, with the *x*-axis corresponding to wavenumber and the *y*-axis to diffraction orders and the vertical FOV. MIR measures up to 20 adjacent diffraction orders for each acquired frame, covering an instantaneous spectral range of 0.15–0.3 μm. Each diffraction order appears as a stripe over the detector, covering around 20 rows. The width of each stripe represents the vertical FOV, and each row is a unique solar occultation spectrum separated by 100-200 m from its adjacent rows.

We use the strong 2.3 μm band for the CO retrieval, which can be measured in positions 6 or 7. Position 7 covers the strongest lines of the 2-0 transitions, located in orders 248–256, and allows measuring CO abundances up to 110 km. Thirty-two ACS MIR occultations have been used to assess the CO vertical distribution during the Global Dust Storm of MY 34 (Olsen et al., 2021). In position 6, the three CO isotopologues (main $C^{12}O^{16}$, $C^{13}O^{16}$, $C^{12}O^{18}$) are measured in orders 246-249 (Figure 3). Position 6 also contains CO_2 and H_2O absorption features, used as a reference in the calibration pipeline. For these reasons, CO monitoring was changed from position 7 to position 6 in November 2018. The line strengths are a little smaller than in Position 7, constraining the measurements of CO up to 90 km. The strongest lines are found in order 249, used for the retrieval.

Calibration of the spectra includes an orthorectification of the detector image, the removal of hot pixels, the dark signal and the straylight, and a correction for the sub-pixel drift occurring due to the slightly varying thermal state of the instrument. The spectral calibration is performed comparing the solar lines with the ACE-FTS solar atlas (Hase et al., 2010), and then refined using atmospheric absorption lines of CO. The instrument line shape is impacted by a doubling (or multiplying) of the image at the detector, originating from an optical anomaly somewhere along the incidence optical path. As a result, many diffraction orders display a doubling of absorption lines. The orders in the bottom part of the detector are mostly free from this effect, and the lines in order 249 located in the lowest part of the detector were preferable. Nevertheless, slight doubling was observed in order 249, and the instrumental function was parameterized using a double gaussian with the fitting of its halfwidth and the relative intensity of two maxima. These parameters are sought for each occultation. A similar approach was described in Alday et al. (2019), Olsen et al. (2021) and Belyaev et al. (2021). The FOV of MIR is small; its vertical resolution is mainly defined by the integration time and amounts to 2.5 km. We averaged ten detector lines near the stripe center for the retrieval, effectively increasing the vertical resolution to 3 km.

The retrieval algorithm of CO from MIR data is similar to that described for the NIR channel. Only two free parameter vectors are retrieved (the H_2O and CO VMRs). The CO_2 absorption band in order 249 is weak and contributes only in the lower atmosphere and at low temperatures. We fixed the CO_2 mixing ratio to 0.96 for the modeling. The HDO/H_2O ratio was assumed constant and equal to 5 (Alday et al., 2021). The pressure and temperature profiles used for constraining spectroscopic parameters are taken from the simultaneous NIR retrievals obtained for the same occultation. The MIR CO vertical profiles for two orbits of MY 34 concurrent with NIR observations are shown in Figure 5C, F.

In case of MIR, the uncertainties of the stray light and the image-doubling made the uncertainties to the instrument line shape (a double peak) and the target altitude. Thanks to the vertical offset of the secondary image, working near the slit edge (in case of order 249) we minimize this problem and contributions of the secondary peak are less than 10% of the primary on average. To test the stability of the retrieval to calibration uncertainties we made the retrieval for each line of the order 249 separately (see fig.S2). The resulting uncertainties of the averaged profile does not exceed 3% and is consistent with the profiles obtained from the averaging of detector lines that showed a stability of results. The second possible bias is the atmospheric temperature and pressure profile used for the retrieval. There is no strong CO_2 band in order 249 and we use NIR temperature-pressure profiles to reduce the uncertainties coming from unknown atmospheric conditions (see fig.S3). The good agreement between NIR and MIR VMR, obtained with different instruments in different absorption bands for the same atmospheric profiles, supports that the uncertainties, coming from calibration and spectroscopy, have been minimized. As was mentioned previously, the NIR temperature can have an uncertainty of 5-7 K. The line strength of the main CO isotopologue ($C^{12}O^{16}$) in spectral range of order 249 has a sensitivity to temperature ~1.5% per Kelvin, it can result in 10% uncertainties of the CO mixing ratio especially in high altitudes where CO lines are not saturated. Finally, we estimate the total systematic uncertainties of the MIR retrieval not exceeding 13%.

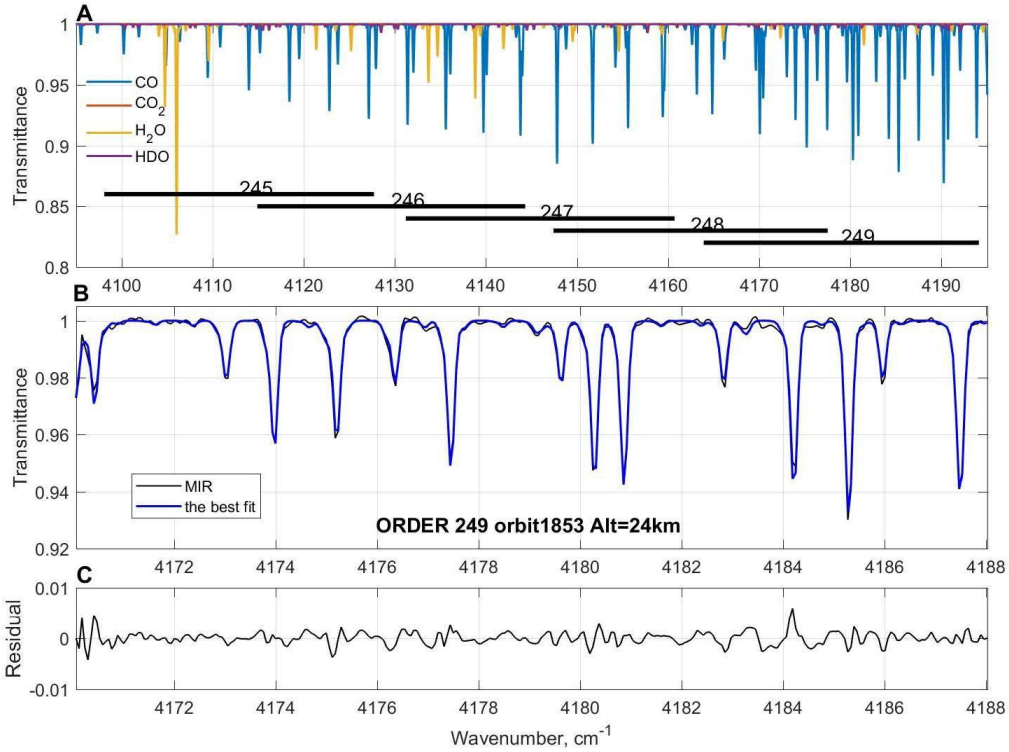

353

354 Figure 3. An example ACS MIR spectrum measured in position 6 at 24 km altitude and the best
355 fit including CO, CO_2 and H_2O contributions. A) the direct model of CO, H_2O, CO_2 and HDO
356 absorption bands in orders 245-249 of position 6. B) spectrum observed at orbit 1853, Ls=164°,
357 81.7°N, 20.5°E and local time of 02:20 (black curve) and the best fit of the data (blue curve); C)
358 residual for the spectrum.

359

360 **2.4 TIRVIM**

361 The thermal infrared (TIRVIM) channel is a Fourier transform spectrometer with solar
362 occultation capability (Korablev et al., 2018; Shakun et al., 2018). TIRVIM operates mainly in
363 the "climatology" mode in solar occultation geometry, covering the entire spectral range from
364 1.7 to 17 μm every 0.4 s, with a spectral resolution of 0.94 cm^{-1}. At 2.8°, the diameter of
365 TIRVIM's circular FOV is larger than the solar disk. The vertical resolution, determined by the
366 angular diameter of the Sun, is close to one atmospheric scale height, varying with Sun-Mars
367 distance from 8.8 to 10.6 km.

368 To retrieve CO from TIRVIM spectra, we used the strongest 4.7 μm band. The low SNR
369 (≤100 only) allows for vertical profile retrievals of CO below 50-60 km (fig. S6). To increase the
370 SNR, four consecutive spectra were averaged. The retrieval algorithm of CO from TIRVIM data
371 is similar to that described for the NIR and MIR channels. The retrieval is sensitive to the
372 atmospheric conditions we have considered (fig. S7-S8). To reduce these uncertainties, we used
373 coinciding NIR temperature profiles available for about 90% of TIRVIM occultations.
374 The main uncertainty of TIRVIM comes from the large FOV (~2.8° equals to ~75 km at the
375 limb). The area of the atmosphere inside FOV is ~60 times higher than the diameter of the Sun.
376 It makes the contribution of aerosol scattering inside FOV not negligible compared to the solar
377 signal especially in the low altitudes. The influence of forward scattered light in transmission
378 measurements of planetary atmospheres has been studied in detail in de Kok and Stam (2012).
379 Based on VIMS Cassini solar occultation measurements of the Titan's atmosphere they showed
380 the gas abundances will be underestimated by about 8% if forward-scattering is ignored in the
381 retrievals. Inside 75 km TIRVIM FOV the aerosol opacity can change by order of magnitude and
382 contribution of different atmospheric layers in the absorption is difficult to predict. To make a
383 valid retrieval of the gaseous absorption in dusty Martian atmosphere the full radiative transfer
384 with the multiple scattering in spherical geometry is needed. It is a difficult problem, given the
385 poorly constrained TIRVIM FOV and it is outside of our current possibility. To minimize this
386 uncertainty, we therefore limited the TIRVIM retrievals to transmittance of 0.8 (the aerosol slant
387 optical depth of ~0.2 at target altitude) and additionally retrieved the CO_2 density from the
388 nearby 4.9 μm CO_2 band because even in this case the contribution of the forward scattering is
389 not excluded due to about 25 km of scattering atmosphere below the solar disc. Finally, CO
390 VMRs of TIRVIM were obtained as the ratio of CO and CO_2 densities.
391 Examples of TIRVIM spectra and fitting are presented in Figure 4, while CO VMR vertical
392 profiles for two orbits in MY 34 are shown in Figure 5C, F.

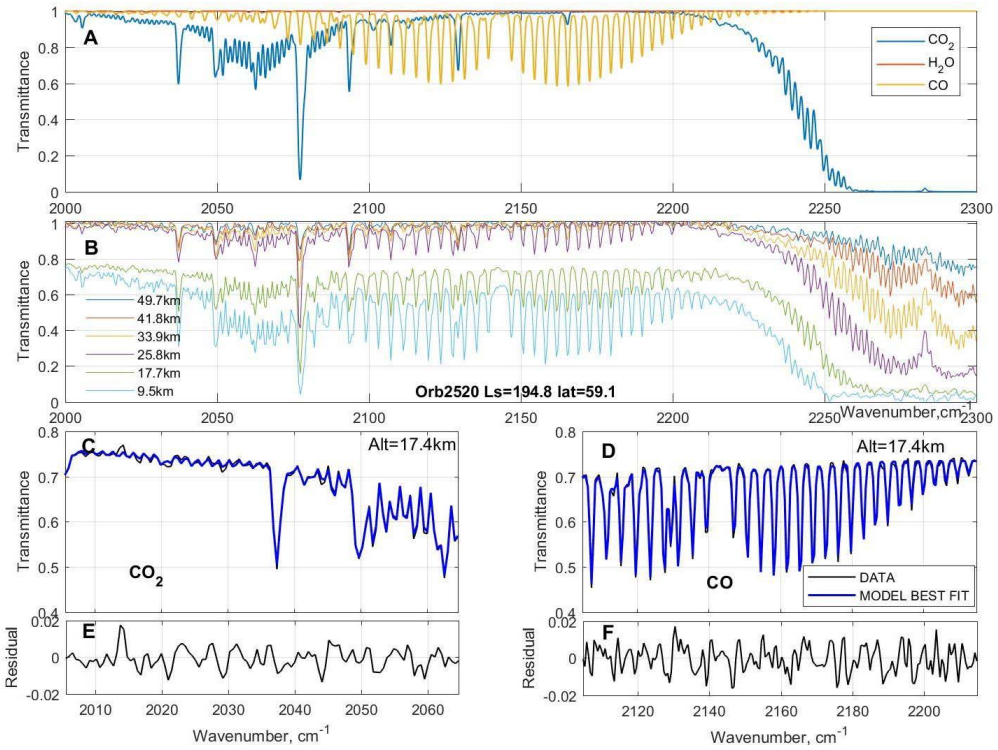

393

394 Figure 4. An example of measured ACS TIRVIM spectrum and its best fit showing the benefit
395 of fitting with a model including both CO_2 and CO. A) the direct model of CO, H_2O, CO_2
396 absorption bands in the spectral range 2000-2300 cm^{-1}. B) spectra observed at different altitudes
397 at orbit 2520, Ls=194.8°, 60.2°N, 167°E and local time of 17:25; C, D) spectrum observed at 17
398 km at the same orbit 2520 (black curve) in the range of CO_2 and CO bands, respectively, and
399 the best fit of the data (blue curve); F, E) residual for the spectrum of CO_2 and CO bands,
400 respectively.

401

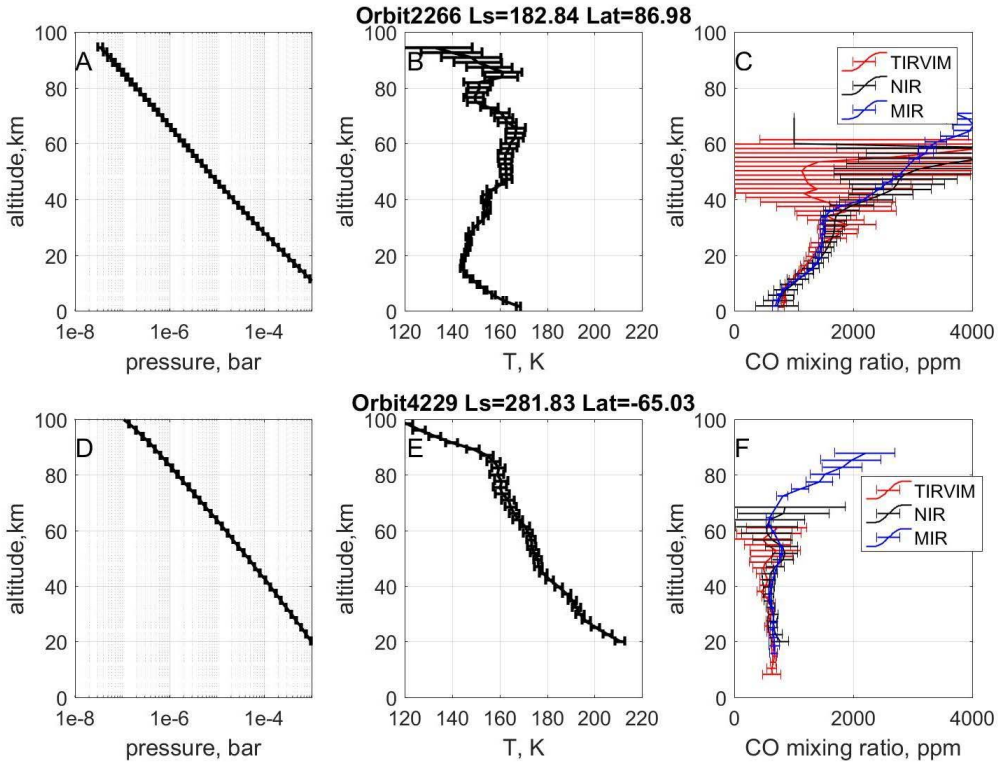

402

403 Figure 5. Example profiles retrieved from ACS NIR-MIR-TIRVIM occultations.

404 A) and D) pressure, derived from the CO_2 number density; B) and E) atmospheric temperature;
405 C) and F) CO profiles from NIR (black), MIR (blue) and TIRVIM (red). The orbits 2266
406 (Ls=182.8°, 87°N, 37.4°E and local time of 7:55) and 4229 (Ls=281.8°, 65.0°S, –74.0°E and
407 local time of 0:21) were completed in northern spring equinox and southern summer solstice,
408 respectively. The retrieved covariance matrix gives the error bars (one-sigma).

409

410

411

412

413

414

3. Results

3.1 Seasonal trend of CO vertical distribution

GCMs predict that CO is expected to be well-mixed from the surface up to ~50 km in mid-and low latitudes (Lefèvre and Krasnopolsky, 2017; Daerden et al., 2019). To verify these theoretical predictions, we considered the evolution of CO measured at two characteristic altitudes, 20 km and 40 km for MYs 34 and 35, as a function of season and latitude (Figure 6). Below 20 km, profiles are strongly attenuated by aerosol extinction. Above 40 km, CO absorption is getting fainter, increasing uncertainty with altitude. However, aerosols frequently prevent accessing altitudes below 30 km (Figure 6A). Thus, the measurements at 20 km are only available in mid-to high-latitudes (30–80°) of both hemispheres. The observations at two altitudes show an apparent difference in VMR and latitudinal variations. The most considerable difference is observed toward the Poles, where downwelling from Hadley cell circulation strongly impacts the shape of the CO VMR vertical profiles, as shown in Olsen et al. (2021).

To follow the evolution of profiles with season and latitude in more detail, we grouped the NIR and MIR data in 30° bins of Ls and presented it as a function of latitude and altitude for both Martian years (Figure 7). Near the solstice in both hemispheres (Ls=60–120º and 240–300º), the latitude coverage is limited to ±60º. In the equinox period (Ls=330–30º and 150–210º), polar latitudes are well covered. Whereas NIR can only measure CO below 50 km, the MIR channel can probe CO up to 90 km in the most favorable cases, a higher altitude range than is accessible for NIR. TIRVIM is not shown here due to poor coverage with altitude and season. The distribution for TIRVIM can be found in the Supporting Information (figure S11).

Overall, the vertical profiles of the CO mixing ratio were found far from being uniform. The minimal values of CO were observed during the southern summer in middle-high southern latitudes. This is consistent with trends observed by CRISM (Smith et al., 2018), PFS (Bouche et al., 2021) and NOMAD (Smith et al., 2021) while the NIR minimal values were within 600–700

ppmv compared to 300–400 ppmv reported by CRISM for latitudes between 70S and 50S (discussed in detail in subsection 3.4). The most prominent feature of the observed profiles is the pronounced maxima of CO VMR at high latitudes. They are present in the lower atmosphere during southern winter and spring and above 40 km near the equinoxes. These polar and mid-latitude enrichments are discussed further in subsections 3.3 and 3.5. In MIR observations, the increase of CO VMR to 3000 ppmv is also observed in the middle and low latitudes above 80 km, indicating the CO_2 photolysis is already efficient at these altitudes. This gradual increase at high altitudes is well supported by one-dimensional models (Krasnopolsky, 2022, fig.5) and was also observed in the first MIR profiles up to 120 km before and after GDS of MY34 (Olsen et al., 2021).

We have also calculated the seasonal distribution of CO with the LMD GCM and its coupled photochemical module in the latest configuration described in Lefèvre et al. (2021). In this dedicated simulation, the GCM is initialized at L_s = 180° of Martian year 33. At this date, CO is set to a uniform (both in altitude and horizontal) initial mixing ratio of 1000 ppmv as previously measured at low latitudes by MIR (Olsen et al., 2021). After a half Martian year of spin-up time, the model runs continuously until the end of Martian year 35 while being constrained by the observed dust climatology (Montabone et al., 2020). The CO vertical distribution calculated by the LMD GCM (Figure 7, left) is in good general agreement with NIR and MIR at low-to-mid latitudes. The increase of CO above 80 km due to the CO_2 photolysis is well predicted. A seasonal minimum is evident in the perihelion season of both years considered here. However, the model largely overestimates the downwelling of thermospheric CO measured during the equinoctial periods at high latitudes. In contrast, near the surface, the strong enrichment of CO measured at high southern latitudes in late winter is absent in the GCM after Ls=150°. This will be also discussed in the following sections.

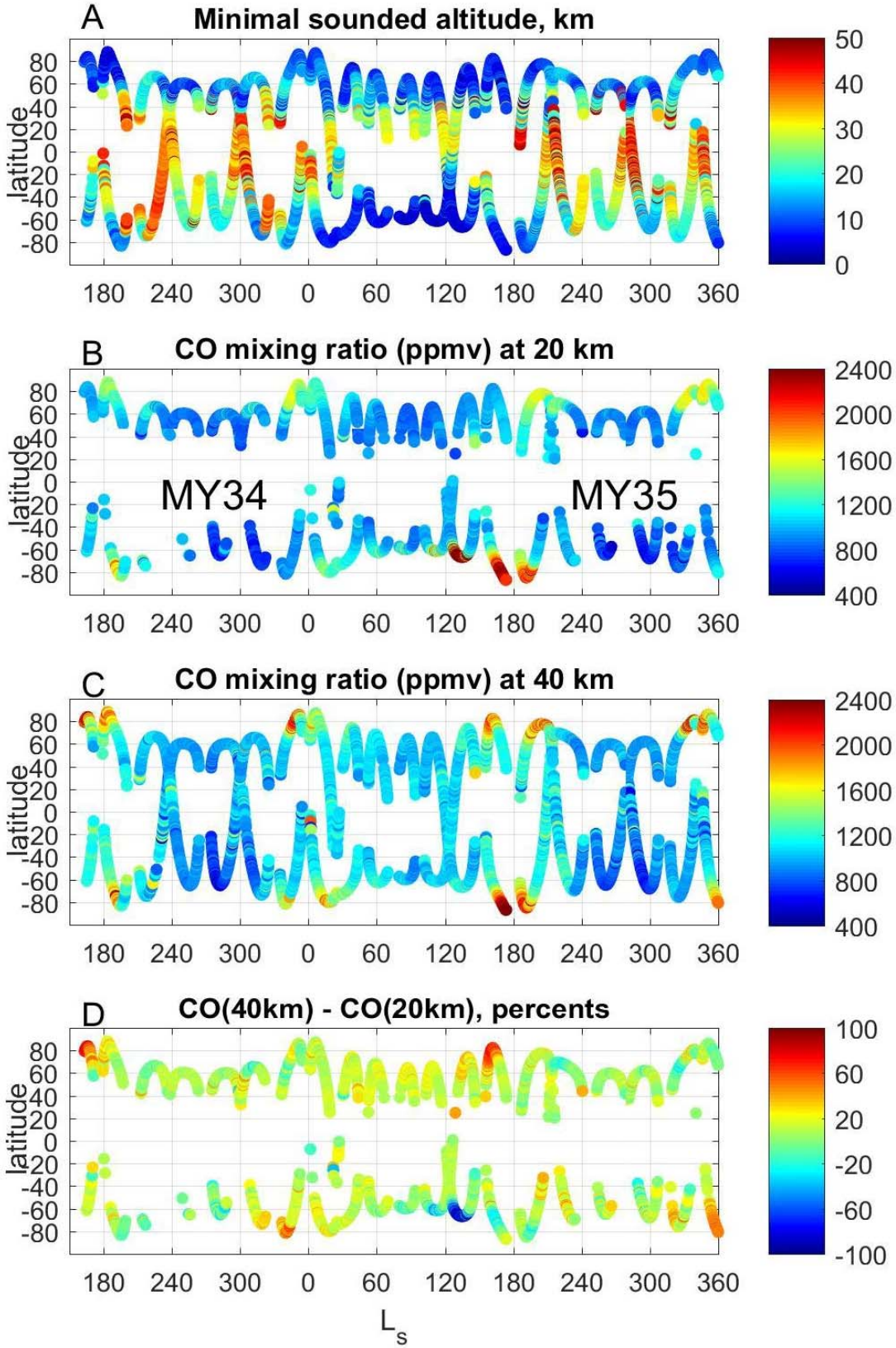

Figure 6. Carbon monoxide mixing ratios (ppmv) from ACS NIR occultations at two altitudes. A) The minimal sounded altitude in km, corresponding to aerosol attenuation of 0.07–0.08; B)

CO VMR at 20 km; C) CO VMR at 40 km; D) relative difference of CO VMR at 40 km and CO VMR at 20 km.

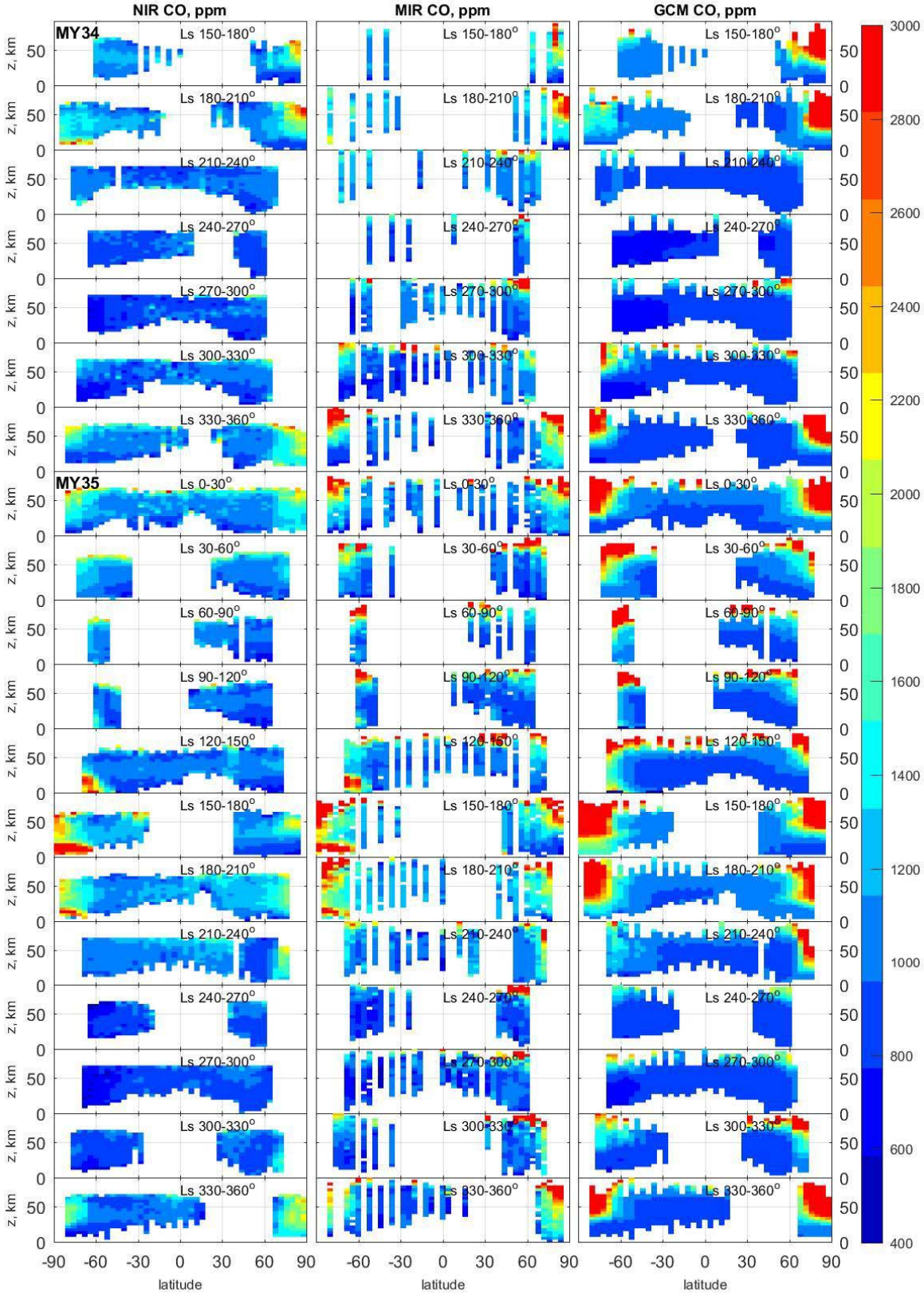
NIR CO, ppm
MIR CO, ppm
GCM CO, ppm
MY34
MY35
Ls 150-180°
Ls 180-210°
Ls 210-240°
Ls 240-270°
Ls 270-300°
Ls 300-330°
Ls 330-360°
Ls 0-30°
Ls 30-60°
Ls 60-90°
Ls 90-120°
Ls 120-150°
z, km
latitude
3000
2800
2600
2400
2200
2000
1800
1600
1400
1200
1000
800
600
400

469

Figure 7. Seasonal distribution of CO mixing ratio observed by ACS NIR (left), ACS MIR (middle) and LMD GCM (right): from MY34 on the top to MY35 on the bottom. Colorbar presents the CO VMR in ppmv.

3.2 The average CO mixing ratio

The global average CO mixing ratio was the focus of many previous observations and 1D modeling studies. The occultation method does not allow sounding the profiles of gases all the way down to the surface due to aerosol opacity of the Martian atmosphere. Figure 6A demonstrates that the minimal sounded altitude in NIR occultations varies from near the surface in polar regions to as high as 40 km at low latitudes. At the same time the global circulation and one-dimensional models predict a uniform CO distribution in the lower atmosphere at low-mid latitudes (Lefevre and Krasnopolsky, 2017, see also S12). To estimate the column-averaged mixing ratio of CO from the ACS profiles, we integrated them from the lowest retrieved altitude to 40 km, where all three spectrometers have good accuracy. To avoid the profiles where aerosol was too opaque in the atmosphere and the lowest retrieved points have big errors due to high slant optical depth and, as a result, low signal, we consider occultations with the minimal altitude (z_{min}) lower than 30 km. We also excluded the polar region and high latitudes where the CO_2 condensation-sublimation cycle and the Hadley circulation make the CO vertical distribution non-uniform (e.g., Figure 6, 7, S12). Thus, we limited ACS measurements to the middle-low latitudes (45°S–45°N). We integrated the CO and CO_2 density profiles from z_{min} to 40 km to get the column abundances. Then the column average CO mixing ratio was obtained as a ratio of column densities, $CO(cm^{-2})/CO_2(cm^{-2})$. Figure 8A shows the seasonal evolution of the column average of CO mixing ratios for the NIR, MIR and TIRVIM measurements, including the earlier results obtained from MIR (Olsen et al., 2021). The CO mean value shows a repeatable seasonal cycle from MY34 to MY35 with two maxima, the first and most prominent at Ls~180° and the second shortly after the spring equinox (Ls=0°) in the Northern hemisphere.

By averaging the Figure 8 data over Ls, we obtain estimates of the annual mean mixing ratio of CO: 970±123 ppmv from NIR, 975±129 ppmv from MIR. In the case of TIRVIM, the annual average equals 852±91 ppmv. The TIRVIM dataset resulted in the lowest average CO VMR and the same was observed for individual occultations (for example around Ls=0 in Fig.8A). TIRVIM has limited Ls coverage (Ls=240° MY 34 to Ls=115° MY 35) and did not probe the two equinox maxima near Ls=180°, resulting in underestimating the annual mean VMR by about 10%, but that is not enough to explain the observed difference. Forward scattering could also be responsible for this difference, even if we try to minimize its impact by choosing altitudes with smaller aerosol slant opacity. Therefore, the three channels of ACS together produce a fairly reliable annual mean for CO of about 960 ppmv.

Figure 8B shows the comparison of ACS results with nadir measurements. NIR, MIR and TIRVIM retrievals for individual occultations were binned within 5° of Ls. PFS/Mars-Express measured CO in the nadir using the 4.7 μm band (Bouche et al., 2021). The data have been taken from the general repository Open Science Framework (Bouche et al., 2020). A selection of PFS data for the same ±45° latitude belt was averaged within 5° bins of Ls for all available Martian years (MY26–33). The seasonal trend agrees well with ACS data. Bouche et al. (2021) calculated a global mean for CO of 820 ppmv. Restricted to the mid-to-low latitudes, the PFS dataset results in a global mean of 844 ppmv, in agreement with TIRVIM results and 15% lower than NIR and MIR values.

Figure 8B presents also the column-averaged CO VMRs retrieved from CRISM and NOMAD by M. D. Smith et al. (2018, 2021) and averaged inside ±40° latitude belt. The annual average in this belt equals ~ 840 ppmv for CRISM and ~800 ppmv for NOMAD, both are lower than our averaged values (Smith et al., 2018; Smith et al., 2021). From ground-based high-resolution observations Krasnopolsky (2015, 2017) obtained an annual mean of 681±13 ppmv, agreeing with the *in situ* measurements by Curiosity yielding 580±80 ppmv (Franz et al., 2015, Trainer et al., 2019).

521 The mean CO mixing ratio calculated by the LMD GCM in Figure 8A shows a very good
522 quantitative agreement with the observations and qualitatively for what concerns the seasonal
523 variation. For both Martian years, the calculated mixing ratio is maximum around Ls = 180°.
524 This is in line with the seasonal evolution of CO at low-to-mid latitudes as measured by nadir-
525 viewing satellites (e.g., Smith et al., 2021; Bouche et al., 2021) and is, more generally, typical of
526 the seasonal evolution of all long-lived non-condensable species (e.g., Trainer et al., 2019). This
527 similarity suggests that the CO_2 condensation-sublimation cycle at polar latitudes is the main
528 driver of the seasonal signal in CO visible in Figure 8. Photochemistry should also play a role in
529 this signal, especially in the CO decrease observed in the perihelion season, when larger amounts
530 of H_2O at all altitudes lead to much increased OH production. The relative contributions of the
531 CO_2 condensation-sublimation and of photochemistry will be studied in a dedicated paper. Also,
532 beyond the scope of the present study is the long-standing problem of the underestimation of CO
533 by models (Lefèvre and Krasnopolsky, 2017), which requires overly lengthy simulations in order
534 to reach the long-term equilibrium value of CO in the GCM. Therefore, this historical problem
535 should not be considered as 'solved' from the sole good agreement found in Figure 8A.
536 Addressing the difference between our observed global mean of 960 ppmv and the nadir
537 results from CRISM, PFS and NOMAD, ~800-840 ppmv, we can consider two possibilities: 1)
538 the geometry of TGO occultations and high aerosol opacity in the Martian atmosphere do not
539 allow us to get good statistics in low latitudes, as seen in figure 6A and SI, and most of the data
540 was obtained at middle latitudes; 2) the reason may be in a sensitivity difference between nadir
541 and occultation instruments and related to the vertical distribution of CO. In nadir, the signal is
542 dominated by absorption from the denser layers and thus by the lowest scale heights below 20-25
543 km. The MIR/NIR vmr average is not exactly a column-average vmr because we can't sound the
544 near-surface mixing ratio at lower latitudes. The minimal sounded altitude (fig 6A) for ACS
545 instruments varies from 2-4 km to 30 km above areoid with an average of 20-21 km, which is
546 above the altitudes that nadir measurements are most sensitive to. If CO increases with altitude

547 below 40 km, the vmr average determined from ACS will be larger than the nadir column-
548 average vmr. This effect should be verified, but we note that except for the polar latitudes in
549 summer (the CO_2 sublimation) the CO vmr in the GCM never decreases close to the surface (fig.
550 S12C) and the standard deviation of CO vmr in low-to-mid latitudes from 0 to 40 km is mostly
551 below 50 ppmv (fig. S12). On the other hand, *Curiosity* measurements on the surface of Mars
552 give 580±80 ppmv (Franz et al., 2015, Trainer et al., 2019) that could indicate near surface
553 values below global average and occultation measurements that are not yet explained in GCMs.

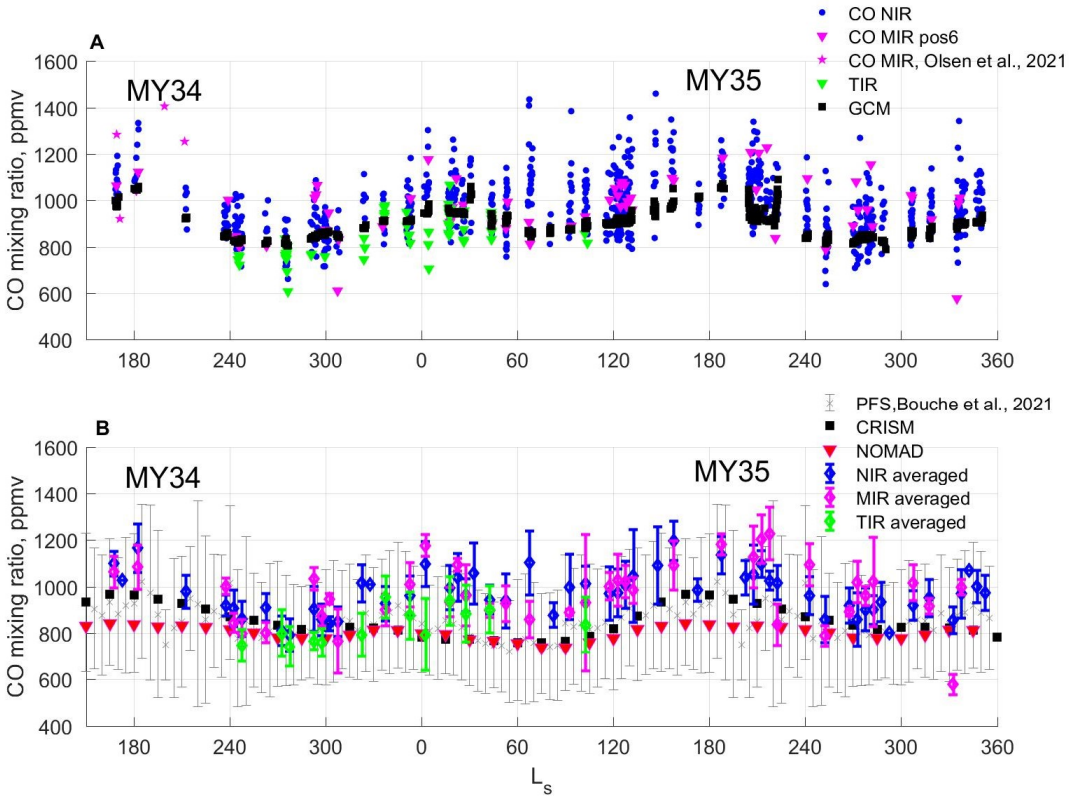

554

555 Figure 8. A) The column-averaged values of CO mixing ratios from ACS profiles measured
556 within ±45° latitude range and below 40 km. Blue points, purple and green triangles are
557 individual NIR, MIR and TIRVIM occultations, respectively. Purple stars are the results of
558 Olsen et al., 2021 from MIR position 7. Black squares are GCM model results corresponding to
559 the NIR averages. B) Blue, purple and green diamonds with error bars are averages of NIR, MIR
560 and TIRVIM data, respectively, binned within 5° of Ls. Grey crosses are averages of PFS data
561 (see text). All error bars are standard deviations. Black squares and red triangles are the column-

562 averaged CO VMRs retrieved from CRISM and NOMAD data, respectively, by M. D. Smith et
563 al. (2018, 2021) and averaged between 40°S and 40°N of latitude. PFS, NOMAD and CRISM
564 data are averaged for all years of observations and do not present specifically MY34 and 35.

565 **3.3 Southern winter-spring CO enhancement**

566 In the lower atmosphere, the maximal values of CO have been observed during the
567 Southern winter/beginning of spring in southern polar latitudes from Ls=120° to 200°. In MY 34
568 the observations began only at Ls=163° and the increase in mixing ratio below 20 km was
569 detected at Ls=187°–195° when the occultations reached high southern latitudes (see Figure 7).
570 In MY35 the coverage was better. The near-surface layer with enhanced CO has been observed
571 from Ls=120° to 195° by both NIR and MIR instruments (Figures 6, 7). Figure 9 shows
572 individual CO profiles of NIR obtained in southern high latitudes at Ls=161°–174° and 185°–
573 195°. A layer of CO at ~10-15 km reached values up to 3000–4000 ppmv (see also fig S13 for
574 MIR and TIRVIM). Twenty-five sols later (Ls=185°) the layer moved to ~15 km with a
575 maximum of 2500–3000 ppmv and then disappeared at Ls≥198°. Above this layer, the CO
576 mixing ratio gradually decreases to 1500-2000 ppmv and then grows again at higher altitudes up
577 to 3000 ppmv. The observed CO maximum correlates with the temperature minimum observed
578 below 30 km at high southern latitudes. At Ls=167°–174° the minimum is observed at 20 km
579 with values as low as 125-135 K 10 km above the CO layer. At Ls=185°–195° the minimum is
580 observed with warmer values about 140-150K.

581 Enhancement of non-condensable species was previously observed in atmospheric argon
582 from measurements of the gamma ray spectrometer (GRS) operated on the Mars-Odyssey orbiter
583 (Sprague et al., 2004, 2007). The strong (a factor of 6) enhancement of Ar was measured over
584 south polar latitudes (75ºS to 90ºS) for two consecutive Mars years near the onset of southern
585 winter close to Ls=90º. In winter over the northern polar regions there was no similar strong
586 enhancement of Ar and the seasonal peak was less obvious than in the south.

587 The nadir measurements of CO showed the strongest CO values at Ls=140º-180º in the
588 southern hemisphere between 45º and 20ºS with mixing ratio about 1100 ppmv (Smith et al.,
589 2018; Smith et al., 2021; Bouche et al., 2021). In case of solar reflected light, the data retrieval
590 was traditionally limited to solar zenith angles (SZA) <80° to avoid the complications of
591 radiative transfer near the limb. That was done for CRISM (Smith et al., 2018). In case of
592 NOMAD the limitation was even higher <55 that is explained by low signal-to-noise ratio of the
593 instrument in nadir (Smith et al., 2021). In turn, PFS observes more thermal radiation, and the
594 observation limitation is driven here by the surface temperatures (too low in polar regions)
595 (Bouche et al., 2021). This could explain why nadir experiments like CRISM, NOMAD and PFS
596 do not show these maximal values at the poles.

597 Unlike nadir, solar occultations can access higher latitudes during the equinox and polar
598 night seasons (>60°S). At Ls=60°–150° of MY35 ACS sounded at the edge of the southern polar
599 night approaching to 65-70°S. During the same period, CRISM, PFS and NOMAD were limited
600 to 30-45°S. CO mixing ratio apparently increased below 20 km at 60°S from 900 to 1500 ppmv
601 during the Ls=90°–120° interval (figure 7). Closer to equinox, occultations moved to higher
602 latitudes where the low-atmospheric layer enriched progressively to 3000 ppmv at Ls=120°–
603 150° (see Figures 7, 8) and then 4000 ppmv at Ls=170°–175° (Figures 8, 9 and S13).

604 In the middle of the southern winter, the column-averaged CO mixing ratio calculated by
605 the LMD GCM reaches more than 4000 ppmv south of 75°S (not shown). However, the region
606 most enriched in CO in the model is located far in the polar night, and only the northernmost tip
607 of the CO-enriched layer near the surface is visible between Ls = 120–150° in Figure 7). In that
608 layer, the modeled enrichment in CO appears to be underpredicted compared to ACS, both in
609 terms of absolute value and vertical extent. Later on, around the equinox, the GCM no longer
610 predicts an enriched layer of CO at high southern latitudes, in strong disagreement with ACS
611 which shows the persistence of an enriched layer in the Ls = 180–210° period. This indicates that
612 the breakup of the polar vortex enriched in CO (and in other non-condensable species) and the

subsequent mixing with midlatitude air occur too early with the settings of the LMD GCM used here.

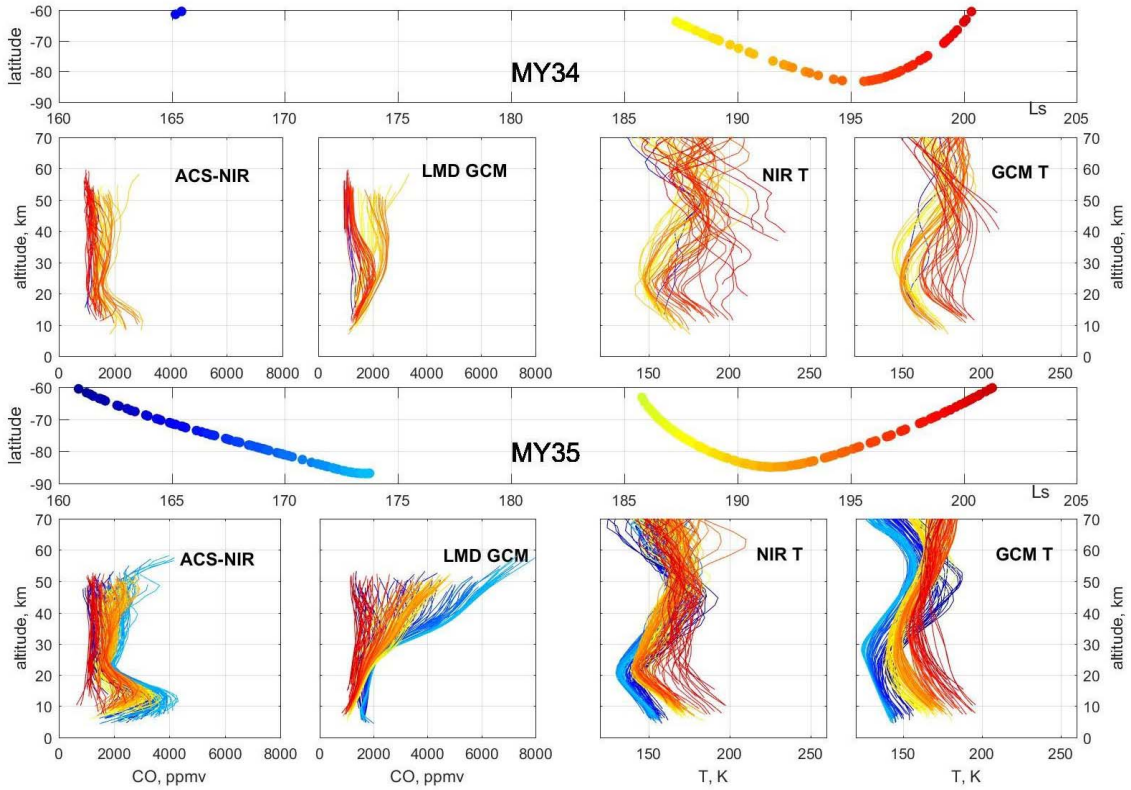

Figure 9. The evolution of the CO mixing ratio profiles for a sequence of occultations in the latitude range 60°S-90°S for martian years 34 and 35. (top) the latitude coverage; (left) ACS NIR measurements; (right) LMD GCM simulation. Colours indicate Ls.

3.4. Southern summer CO depletion

CRISM observations, followed later by PFS and NOMAD nadir measurements, observed a minimum of CO abundance during the southern summer. This depletion was related to the sublimation of the southern CO_2 polar cap and resulted in the strong decrease of the CO column mixing ratio to the 300-500 ppmv from Ls=210° to Ls=330° in the high and middle southern latitudes (Smith et al., 2018, 2021).

In Figure 6b at 20 km, the CO depletion is seen in both MY 34 and 35 between Ls 250° and 330° in the southern hemisphere. During this period, Mars' GCM predicts a non-uniform vertical distribution with strong vertical gradient and depletion near the surface (Holmes et al., 2019). So, we decided to investigate the CO vertical distribution for the both observed southern summer seasons in more detail.

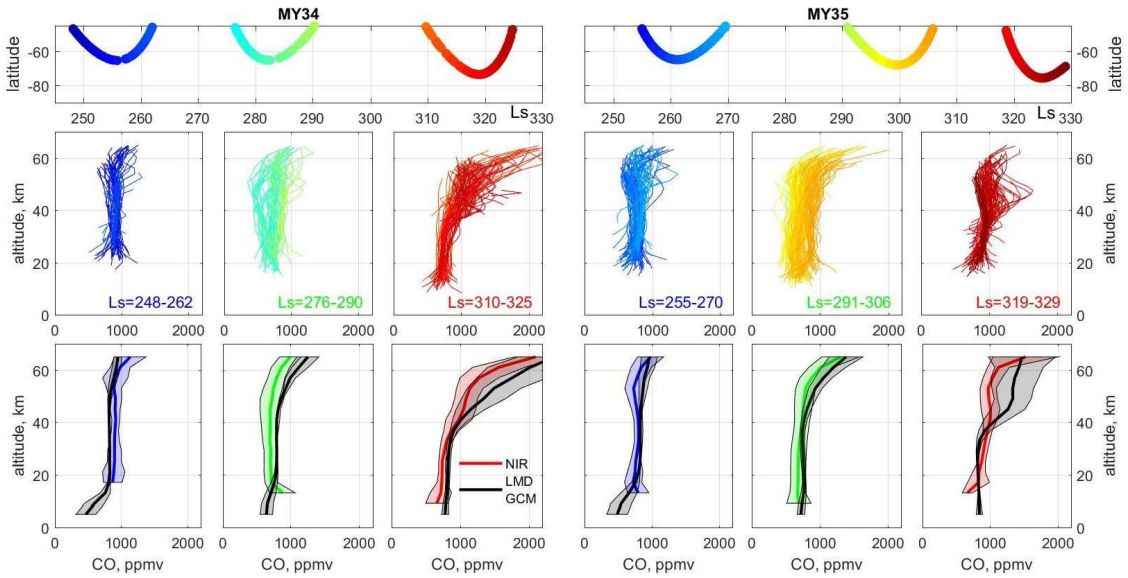

Figure 10. The evolution of the CO mixing ratio profiles for a sequence of occultations in the latitude range 45°S–90°S and Ls from 245° to 330° for MY 34 and 35; (top) the latitude coverage; (middle) ACS NIR individual profiles for Ls bins; (bottom) the averaged profile for each Ls bin for ACS NIR and GCM LMD. The shaded area is the standard deviation.

Figure 10 presents the evolution of the CO profiles in the latitude range from 45°S to 90°S and in the period from Ls=245 to 330° for both Martian years (34 and 35). In this dusty season, solar occultation can not sound deep in the atmosphere and the lowest altitude sounded is typically 20 km above the surface except for Ls=310°–325° of MY34 and Ls=291°–306° in MY35 where we could probe down to 10 km. For both years we do not see a prominent gradient below 40 km except at Ls=309–325° of MY 34 where nearly-constant mixing ratios were observed below 35 km, with an increase above. The average CO mixing ratio below 40 km was

found to be 700–750 ppmv which is higher than those obtained by CRISM and NOMAD between 50°S and 70°S (400 ppmv at Ls=260° and 700 ppmv at Ls=330° for CRISM and 500 ppmv at Ls=260° and 650-700 ppmv at Ls=330° for NOMAD) and by PFS in the same period (~600 ppmv). This difference can be related again to the altitude sensitivity of nadir and occultation measurements. To test it, we compared the CO profiles calculated in summer by the LMD GCM with ACS measurements (fig.10, bottom panels). Above 20 km, where the observations are available, the model and data are in broad agreement. But below 20 km, the model shows a smooth decrease of the mixing ratio to the surface due to the sublimation in the southern summer at Ls=250-270° that could explain a huge difference between ACS and nadir measurements for this period. The model profiles tend also to anticipate the downwelling of enhanced CO mixing ratios by the Hadley circulation at the approach of the equinox (Ls = 318–330° in Figure 10).

3.5 High altitude equinox and solstice enhancement

The enhancement of CO at 50 km was first observed by Krasnopolsky (2014) based on CO (2-1) dayglow observations at 4.7 μm in the middle of northern summer (Ls=110°) using the CSHELL spectrograph at NASA IRTF. This dayglow is formed by CO molecules at 50 km. The mixing ratio was found to increase from 1100 ppm at 40°S to 1600 ppm at 70°N. This behavior was different from the trend observed at low altitudes and was therefore attributed to the Hadley circulation characterized by the equator-to-pole Hadley cells in equinox and pole-to-pole cell in solstices. This circulation transports CO to the polar region where a downward flux of CO-rich air occurs.

The NIR and MIR observations in the same period also support the increase of the CO mixing ratio in the polar region above 50 km but the mixing ratio is much smaller than in the model (Figure 7). The most sensitive for the study is the MIR spectrometer that can measure CO up to 80 km and has better accuracy compared to NIR at altitudes between 50 and 60 km (see

671 section 2 and SM). Figure 11 presents the observed and modeled mixing ratio profiles of CO in
672 both hemispheres at latitudes from 70° to 90° over time periods that encompasses equinoxes.
673 The equinoctial circulation is characterized by two symmetric Hadley cells facing each other
674 about the equator and carrying airmasses from the equator to the poles. The equinox periods
675 covered concern Ls=150° to 210° (MY35) for the northern spring and Ls=330°–30° (MY 34/35)
676 for the southern spring. Before and after these ranges, the maxima are also observed, but the
677 circulation is already being rearranged. These maxima especially in low-to-middle latitudes are
678 located mostly higher than 60 km and are related to the increase of the CO mixing ratio due to
679 the CO_2 photolysis.

680 At both equinoxes, the model is in rather good agreement with ACS at latitudes about
681 70°, but overestimates CO when moving to the poles. In the northern spring of MY34 and 35 the
682 observed profiles have shown a weak gradient from 1000 ppm at 10 km to 2000–3000 ppm at 60
683 km depending on latitude with smaller values at lower latitudes. Above 60 km and at latitudes
684 higher than 80°N the sharp increase of CO is visible at high latitudes to 5000 ppm at 80 km. The
685 GCM profiles begin to grow from 30 km and overestimate the CO VMR above this altitude by at
686 least a factor of 2 compared to observations. For instance, the modeled CO VMR reached 8000-
687 10000 ppmv at 70-80 km. The same situation is observed in the southern spring except near the
688 surface CO layer discussed in Section 3.3. In the southern and northern autumn of MY34 and 35,
689 respectively, the CO mixing ratio changes from 1000 ppmv at 10 km to 4000 ppmv at 70 km but
690 with a sharper gradient compared to the spring. The model begins to overestimate the data in
691 some cases from 20 km. This suggests that the intensity of the Hadley cells at the equinox is too
692 strong in the GCM, bringing too much CO from its region of production in the high atmosphere.

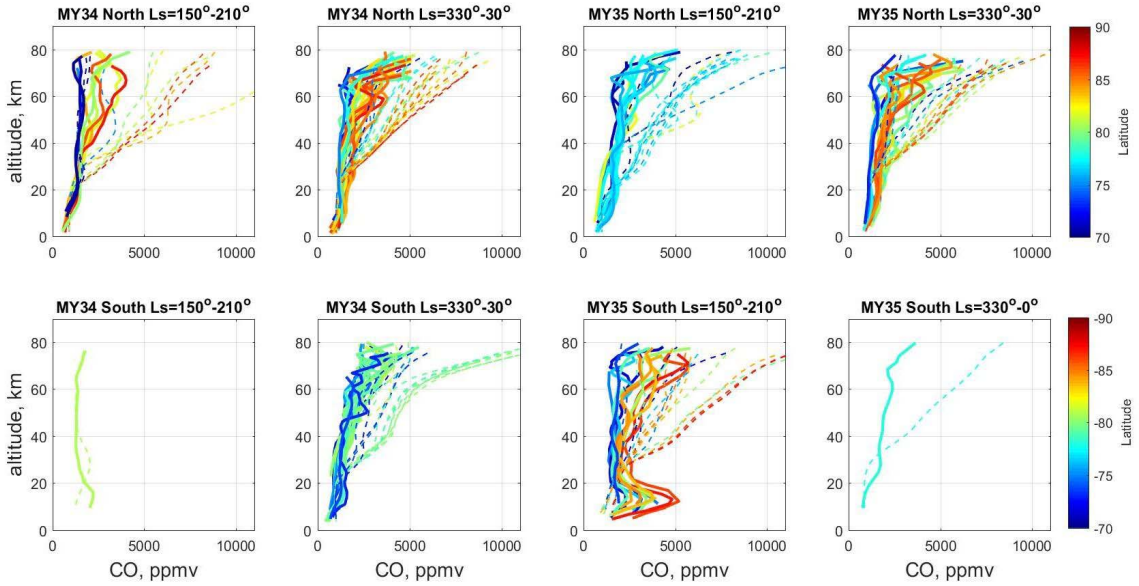

693

694 Figure 11. The evolution of the CO mixing ratio profiles for sequence of occultations for
695 equinox season (Ls=150°–210° and 330°–30°) for MY 34 and 35 in high southern and northern
696 latitudes (–70° to –90° and 70° to 90°, respectively). Colors indicate the latitude variations. Solid
697 curves are the ACS MIR data, dashed curves represent the LMD GCM simulation.

698

699 ***3.6 Interannual variability due to the GDS of MY 34***

700 In the lower atmosphere, provided there is water vapor, the loss of CO by reaction with
701 OH exceeds its production. It should then end up making CO sensitive to changes in water
702 content. Nevertheless, the lifetime of about five terrestrial years does not authorize prominent
703 chemical variations of CO at the seasonal timescales.

704 MY 34 was characterized by the GDS that began at approximately Ls=185° (Guzewith et
705 al., 2019; Smith, 2019) in the Northern hemisphere. The first phase of the storm from Ls=185º to
706 192° is better defined as a regional dust storm which then turned into a massive global event at
707 Ls=197° after the secondary massive dust injection over Tharsis (Montabone et al., 2020). The
708 decay phase of the storm started at Ls=210° and lasted until Ls=240°. It is now known that GDSs
709 profoundly impact water vertical distribution in the atmosphere by transferring H_2O to high
710 altitudes (Fedorova et al., 2018; 2020, 2021; Heavens et al., 2018; Aoki et al., 2019, Belyaev et

al 2021). Dust heats the atmosphere and amplifies the Hadley cell circulation which in turn increases the altitude of the hygropause. The water vertical distribution during the GDS of MY 34 was studied with ACS and NOMAD on TGO (Fedorova et al., 2020; Aoki et al., 2019; Belyaev et al., 2021) and SPICAM (SPectroscopy for the Investigation of the Characteristics of the. Atmosphere of Mars) on Mars Express using the solar occultation technique (Fedorova et al., 2021). Water was observed up to 120 km with mixing ratios of 20–50 ppmv. More water in the middle atmosphere provides more OH (hydroxyl) radicals once H_2O is photolyzed. This has the effect of boosting the rate of reactions between CO and OH, and hence the reformation of CO_2. So, the sensitivity of CO to water activity can provide an insight into the stability of the Martian atmosphere.

The first ever profiles of CO were produced by ACS MIR and reported for the period from Ls=163° (pre-storm) to Ls=220° (decay phase), which showed how CO was affected by this event (Olsen et al., 2021). After the onset of the dust storm, the mean CO mixing ratio was observed to decrease from 1260 to 1070 ppmv below 40 km which was explained as the enhanced presence of H_2O and thus OH that subsequently accelerated CO loss. The same occurred at high altitudes where the rise of hygropause also resulted in the decrease of CO.

With two Martian years of observations, we can compare the CO vertical profiles during the GDS period of MY 34 with the more regular MY 35 using ACS NIR data. The panels of Figure 7 at Ls=180°–210° clearly show more CO in the high southern latitudes during MY 35 than during MY 34. On the other hand, CO in high northern latitudes at altitudes above 40 km is more abundant in MY 34. Over Ls=210°–240°, the observed CO mixing ratios between 30 and 60 km in low latitudes (30°S–30°N) is higher in MY 35 compared to MY 34. As shown in Figure 1, solar occultations in different years can have different latitudinal distributions and the observations can relate to different Ls. To exclude these uncertainties, we have selected smaller latitude bins than in Figure 7 (10°of Ls versus 30° of Ls) to compare nearly close in Ls and latitude observations for two years (Figure 12). We average the ACS dataset inside 10° of Ls,

737 10° of latitude and 10 km of altitude. In Figure 12 the CO values for the selected bins are shown
738 as altitude-latitude maps for MY 34 and MY 35 together with their relative difference, where the
739 Ls-latitude coverage permits.
740
741

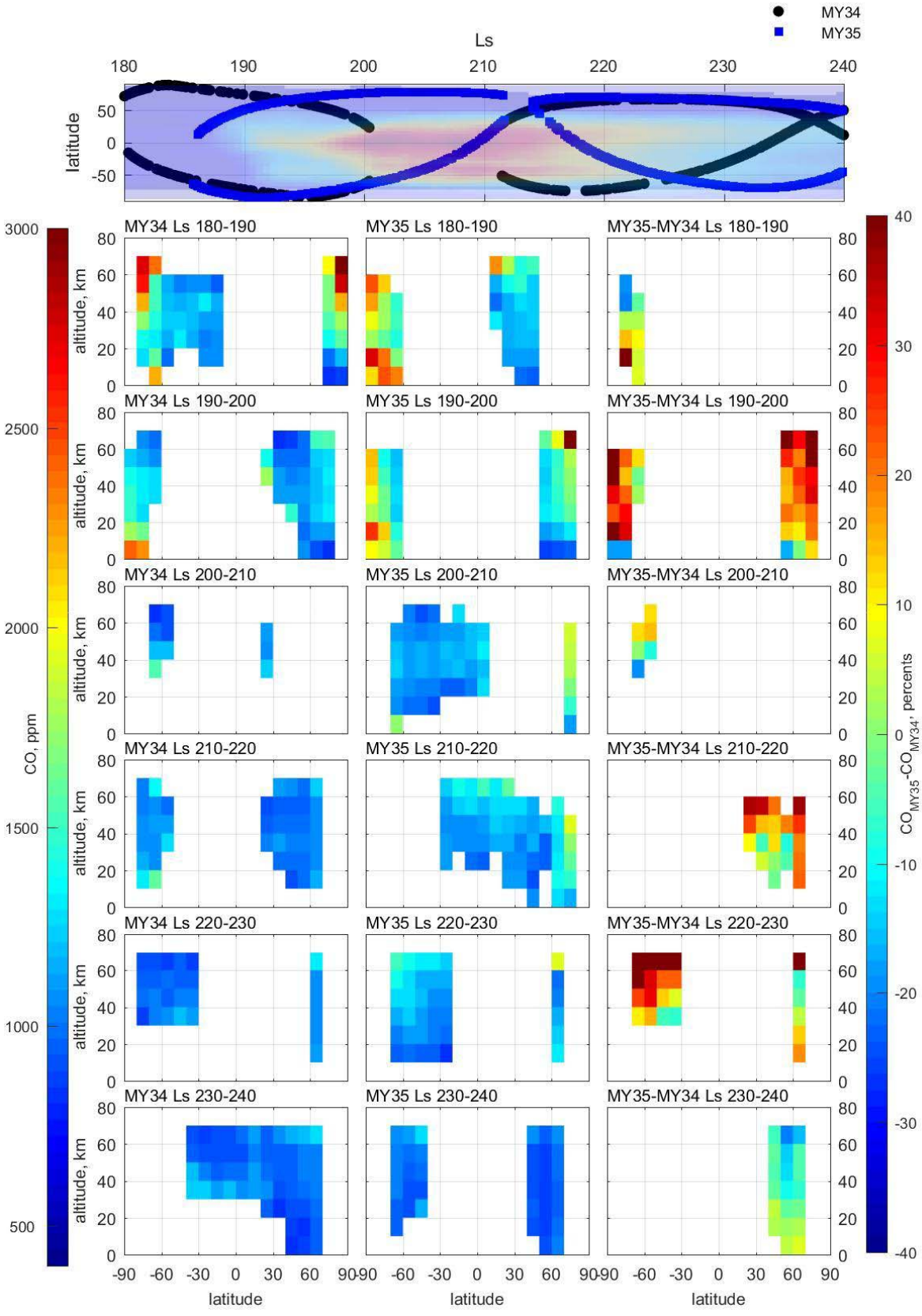

742

743 Figure 12. The latitudinal trend of the CO mixing ratio vertical profiles in ppmv into 10° Ls bins

744 from Ls=180° to 240° for MY34 (left) and MY35 (middle) and their relative difference in

745 percent (right). On the top panel is the seasonal distribution of ACS NIR solar occultation
746 observations for MY 34 and 35 at Ls=180–240°. The colored background is the dust optical
747 depth distribution in 9 μm for MY 34 from Montabone et al. (2020) with red color corresponding
748 to maximal optical depth and blue color corresponding to minimal.
749
750 For the first Ls bin (180°–190°) the data from the two years overlap only in high southern
751 latitudes just before the beginning of GDS and the difference near 60°S does not exceed 10%.
752 From Ls=190° to 230°, during the maximal dust loading, the CO mixing ratio in MY 35 is larger
753 than in MY 34 of 30–40% both in the northern and southern hemispheres. On the decay of GDS,
754 at Ls=230°–240°, the observations overlap in middle northern latitudes, and the difference
755 between two years was within 10% again. This depletion of the CO mixing ratio is well
756 supported by LMD GCM modeling for MY 34 and 35 with corresponding dust scenario (see
757 Figure S15). The decrease of the CO mixing ratio in MY 34 during the GDS is also anti-
758 correlated with increase of water vapor abundance in the atmosphere in both hemispheres for the
759 same period (see Figure S16). The notable CO depletion during the GDS of MY 34 can indicate
760 the response of CO_2 production rate to the strong increase in water vapor during this period (see.,
761 e.g. Fedorova et al., 2020).
762
763 **Conclusions**
764 We analyzed a large dataset of CO vertical profiles made using solar occultation
765 observations of the three ACS spectrometers onboard the ExoMars Trace Gas Orbiter. The data
766 has been collected from April 2018 (Ls=163° of MY 34) to March 2021 (Ls=360° of MY 35)
767 and covers 1.5 Martian years. The densest dataset comes from the ACS NIR spectrometer, which
768 collected more than 6200 occultations over this period. For this dataset, we made the
769 simultaneous retrieval of vertical profiles of pressure, temperature, and CO mixing ratio over
770 altitudes from 0 to 60 km, and in the spectral range of 1.582-1.567 μm (order 49 of the

771 spectrometer), which includes the 1.57 μm CO_2 band and the CO (3-0) overtone at 1.57 μm.
772 ACS TIRVIM provides the second densest dataset of about 1000 occultations, but these
773 observations stopped in December 2019. The CO mixing ratio was retrieved based on the strong
774 4.7 μm CO absorption band and the CO_2 density from 4.9 μm band. The low SNR and spectral
775 resolution limit the sounding altitude to below 50 km. ACS MIR, the most sensitive channel of
776 ACS, has performed 620 occultations up to the end of MY 35 and provided the measurements of
777 CO VMR vertical profiles in 2.3 μm absorption band based on CO_2 density and temperature
778 retrieved from simultaneous measurements of ACS NIR in the range of altitude from 0 to 80 km.
779 With this dataset we presented the first detailed analysis of CO vertical distribution over
780 a long timescale and studied seasonal and latitudinal variations during a Martian year:
781 1) We found a mean CO VMR of ~ 960 ppmv in the range of 10-35 km and in the low and
782 middle latitudes (from 45°S to 45°N). Our averaged values are higher than the CRISM,
783 NOMAD and PFS/MEX global averages from nadir measurements, all three being of ~
784 800 ppmv (Smith et al., 2018; Smith et al., 2021; Bouche et al., 2021). This difference
785 can be related to different sensitivity of nadir and occultation measurements. The CO
786 mean value shows a repeatable seasonal cycle from MY 34 to MY 35 with two maxima,
787 the first and largest of the two at Ls~180° and the second shortly after spring equinox
788 (Ls=0°) in the Northern hemisphere.
789 2) We found a strong enrichment of CO near the surface during the southern winter and
790 spring (Ls=100–200°) in middle and high southern latitudes with a layer of 3000-4000
791 ppm at 10-20 km corresponding to local depletion of CO_2. In the Northern polar winter
792 atmosphere, such a strong layer of CO was not observed. The GCM does not predict the
793 enrichment in CO in this period, both in terms of absolute value and vertical extent. This
794 indicates that the breakup of the polar vortex enriched in CO (and in other non-
795 condensable species) and the subsequent mixing with mid-latitude air occur too early
796 with the settings of the LMD GCM used here.

3) In the equinox seasons both in the northern and southern spring, we found an increase of CO mixing ratio above 50 km to 3000–4000 ppmv which is related to the downwelling flux of the equinox Hadley circulation on Mars above the Poles enriched of CO molecules. The comparison with the general circulation chemical model has shown that it tends to overestimate the intensity of this process, bringing too much CO from its region of production in the high atmosphere.

4) The minimum of CO observed in the southern summer in the high and middle southern latitudes has average VMRs of 700–750 ppmv in the low atmosphere and agrees well with nadir measurements by CRISM/MRO and PFS/MEX even they have lower values of 400-700 ppmv and ~600 ppmv, respectively, in the same period that can be also explained by different altitude sensitivity of nadir and occultation observations The CO profiles calculated in southern summer by the LMD GCM are in broad agreement with ACS.

5) The observations during the two Martian years allow us to study the interannual variability for a year with a global dust storm (MY 34) and a year without (MY 35). We observed the depletion of the CO mixing ratio at 30-40% both in the northern and southern hemispheres during the global dust storm of MY 34 compared with the calmer MY 35. The decrease of the CO mixing ratio in MY 34 can indicate the response of CO_2 production rate to the increase of water vapor abundance in the atmosphere for the same period that suggests an impact of HO_x chemistry on the CO abundance.

Acknowledgments

The ExoMars mission is a joint mission of the European Space Agency (ESA) and Roscosmos. The ACS experiment is led by the Space Research Institute (IKI) in Moscow, assisted by LATMOS in France. The science operations of ACS are funded by Roscosmos and ESA. Authors affiliated with IKI acknowledge funding from the Ministry of Science and High

Education of Russia. Authors affiliated with LATMOS acknowledge funding from CNES and Centre National de la Recherche Scientifique (CNRS). Authors affiliated with the University of Oxford acknowledge funding from the UK Space Agency under grants ST/T002069/1, ST/R001502/1 and ST/P001572/1. We thank our reviewers for helpful comments that improved the manuscript a lot.

Data availability.

ACS data are available from ESA Planetary Science Archive (PSA) Level 2 https://archives.esac.esa.int/psa/#!Table%20View/ACS=instrument. The CO vertical profiles generated from ACS measurements and analyzed in this study are available at Fedorova (2022).

Reference

Alday, J., Trokhimovskiy, A., Irwin, P. G. J., Wilson, C. F., Montmessin, F., Lefévre, F., et al. (2021). Isotopic fractionation of water and its photolytic products in the atmosphere of Mars. *Nature Astronomy*, *5*(9), 943–950. https://doi.org/10.1038/s41550-021-01389-x

Alday, J., Wilson, C. F., Irwin, P. G. J., Olsen, K. S., Baggio, L., Montmessin, F., et al. (2019). Oxygen isotopic ratios in Martian water vapour observed by ACS MIR on board the ExoMars Trace Gas Orbiter. *Astronomy & Astrophysics*, *630*, A91. https://doi.org/10.1051/0004-6361/201936234

Aoki, S., Vandaele, A. C., Daerden, F., Villanueva, G. L., Liuzzi, G., Thomas, I. R., et al. (2019). Water Vapor Vertical Profiles on Mars in Dust Storms Observed by TGO/NOMAD. *Journal of Geophysical Research: Planets*, *124*(12), 3482–3497. https://doi.org/10.1029/2019je006109

Belyaev, D. A., Fedorova, A. A., Trokhimovskiy, A., Alday, J., Montmessin, F., Korablev, O. I., et al. (2021). Revealing a High Water Abundance in the Upper Mesosphere of Mars With ACS Onboard TGO. *Geophysical Research Letters*, *48*(10), e2021GL093411. https://doi.org/10.1029/2021GL093411

Billebaud, F., Brillet, J., Lellouch, E., Fouchet, T., Encrenaz, T., Cottini, V., et al. (2009). Observations of CO in the atmosphere of Mars with PFS onboard Mars Express. *Planet. Space Sci.*, *57*, 1446–1457. https://doi.org/10.1016/j.pss.2009.07.004

Billebaud, F., Maillard, J. P., Lellouch, E., & Encrenaz, T. (1992). The spectrum of Mars in the (1-0) vibrational band of CO. *Astronomy and Astrophysics*, *261*, 647–657.

Billebaud, F., Rosenqvist, J., Lellouch, E., Maillard, J.-P., Encrenaz, T., & Hourdin, F. (1998). Observations of CO in the atmosphere of Mars in the (2-0) vibrational band at 2.35 microns. *Astronomy and Astrophysics*, *333*, 1092–1099.

Bouche, J., Bauduin, S., Giuranna, M., Robert, S., Aoki, S., Vandaele, A. C., et al. (2019). Retrieval and characterization of carbon monoxide (CO) vertical profiles in the Martian atmosphere from observations of PFS/MEX. *Journal of Quantitative Spectroscopy and Radiative Transfer*, *238*, 106498. https://doi.org/10.1016/j.jqsrt.2019.05.009

Bouche, J., Coheur, P.-F., Giuranna, M., Wolkenberg, P., Nardi, L., Amoroso, M., … Bauduin, S. (2020, April 15). Data: "Seasonal and spatial variability of carbon monoxide (CO) in the Martian atmosphere from

PFS/MEX observations." Retrieved from https://osf.io/xsknv/?view_only = 47d671dd84d84fe4b8802c726d293b4c.

Bouche, J., Coheur, P.-F., Giuranna, M., Wolkenberg, P., Nardi, L., Amoroso, M., et al. (2021). Seasonal and Spatial Variability of Carbon Monoxide (CO) in the Martian Atmosphere From PFS/MEX Observations. *Journal of Geophysical Research: Planets*, *126*(2), e2020JE006480. https://doi.org/10.1029/2020JE006480

Ceccherini, S., (2005). Analytical determination of the regularization parameter in the retrieval of atmospheric vertical profiles, *Opt. Lett. 30*, 2554-2556.

Clancy, R. T., Muhleman, D. O., & Berge, G. L. (1990). Global changes in the 0–70 km thermal structure of the Mars atmosphere derived from 1975 to 1989 microwave CO spectra. *Journal of Geophysical Research: Solid Earth*, *95*(B9), 14543–14554. https://doi.org/10.1029/JB095iB09p14543

Daerden, F., Neary, L., Viscardy, S., García Muñoz, A., Clancy, R. T., Smith, M. D., et al. (2019). Mars atmospheric chemistry simulations with the GEM-Mars general circulation model. *Icarus*, *326*, 197–224. https://doi.org/10.1016/j.icarus.2019.02.030.

de Kok, R.J., Stam, D.M. (2012). The influence of forward-scattered light in transmission measurements of (exo)planetary atmospheres. *Icarus, 221(2)*, 517-524. https://doi.org/10.1016/j.icarus.2012.08.020.

Encrenaz, T., Fouchet, T., Melchiorri, R., Drossart, P., Gondet, B., Langevin, Y., et al. (2006). Seasonal variations of the martian CO over Hellas as observed by OMEGA/Mars Express. *Astron. Astrophys.*, *459*, 265–270. https://doi.org/10.1051/0004-6361:20065586

Fedorova, A., Bertaux, J. L., Betsis, D., Montmessin, F., Korablev, O., Maltagliati, L., & Clarke, J. (2018). Water vapor in the middle atmosphere of Mars during the 2007 global dust storm. *Icarus*, *300*, 440–457. https://doi.org/10.1016/j.icarus.2017.09.025

Fedorova, A. A., Montmessin, F., Korablev, O., Luginin, M., Trokhimovskiy, A., Belyaev, D. A., et al. (2020). Stormy water on Mars: The distribution and saturation of atmospheric water during the dusty season. *Science*, *367*(6475), 297–300. https://doi.org/10.1126/science.aay9522

Fedorova, A., Montmessin, F., Korablev, O., Lefèvre, F., Trokhimovskiy, A., & Bertaux, J.-L. (2021). Multi-Annual Monitoring of the Water Vapor Vertical Distribution on Mars by SPICAM on Mars

Express. *Journal of Geophysical Research: Planets*, *126*(1), e2020JE006616. https://doi.org/10.1029/2020JE006616

Fedorova, A. (2022). "Carbon monoxide (CO) on Mars from ACS occultations (MY34-35)", Mendeley Data, V2, doi: 10.17632/w2b89yr6x5.2.

Forget, F., Hourdin, F., Fournier, R., Hourdin, C., Talagrand, O., Collins, M., et al. (1999). Improved general circulation models of the Martian atmosphere from the surface to above 80 km. *J. Geophys. Res.*, *104*, 24155–24176. https://doi.org/10.1029/1999JE001025

Forget, F., Millour, E., Montabone, L., & Lefevre, F. (2008). Non Condensable Gas Enrichment and Depletion in the Martian Polar Regions, *1447*, 9106. Presented at the Third International Workshop on The Mars Atmosphere: Modeling and Observations.

Franz, H. B., Trainer, M. G., Wong, M. H., Mahaffy, P. R., Atreya, S. K., Manning, H. L. K., & Stern, J. C. (2015). Reevaluated martian atmospheric mixing ratios from the mass spectrometer on the Curiosity rover. *Planetary and Space Science*, *109–110*, 154–158. https://doi.org/10.1016/j.pss.2015.02.014

Gordon, I. E., Rothman, L. S., Hill, C., Kochanov, R. V., Tan, Y., Bernath, P. F., et al. (2017). The HITRAN2016 molecular spectroscopic database. *J. Quant. Spectrosc. Radiat. Transfer*, *203*, 3–69. https://doi.org/10.1016/j.jqsrt.2017.06.038

Guzewich, S. D., Lemmon, M., Smith, C. L., Martínez, G., Vicente-Retortillo, Á. de, Newman, C. E., et al. (2019). Mars Science Laboratory Observations of the 2018/Mars Year 34 Global Dust Storm. *Geophysical Research Letters*, *46*(1), 71–79. https://doi.org/10.1029/2018GL080839

Hase, F, Wallace, L., McLeod, S.D., Harrison, J.J, Bernath, P.F. (2010). The ACE-FTS atlas of the infrared solar spectrum, *Journal of Quantitative Spectroscopy and Radiative Transfer, 111 (4),* 521-528. https://doi.org/10.1016/j.jqsrt.2009.10.020.

Heavens, N. G., Kleinböhl, A., Chaffin, M. S., Halekas, J. S., Kass, D. M., Hayne, P. O., et al. (2018). Hydrogen escape from Mars enhanced by deep convection in dust storms. *Nature Astronomy*, *2*(2), 126–132. https://doi.org/10.1038/s41550-017-0353-4

Holmes, J. A., Lewis, S. R., Patel, M. R., & Smith, M. D. (2019). Global analysis and forecasts of carbon monoxide on Mars. *Icarus*, *328*, 232–245. https://doi.org/10.1016/j.icarus.2019.03.016

Kaplan, L. D., Connes, J., & Connes, P. (1969). Carbon Monoxide in the Martian Atmosphere. *Astrophys.*

J., *157*, L187. https://doi.org/10.1086/180416

Korablev, O., Montmessin, F., Trokhimovskiy, A., Fedorova, A. A., Shakun, A. V., Grigoriev, A. V., et al. (2018). The Atmospheric Chemistry Suite (ACS) of Three Spectrometers for the ExoMars 2016 Trace Gas Orbiter. *Space Science Reviews*, *214*(1), 7. https://doi.org/10.1007/s11214-017-0437-6

Krasnopolsky, V. A. (2003). Spectroscopic mapping of Mars CO mixing ratio: Detection of north-south asymmetry. *J. Geophys. Res.*, *108*, 5010. https://doi.org/10.1029/2002JE001926

Krasnopolsky, V. A. (2007). Long-term spectroscopic observations of Mars using IRTF/CSHELL: Mapping of O_2 dayglow, CO, and search for CH_4. *Icarus*, *190*, 93–102. https://doi.org/10.1016/j.icarus.2007.02.014

Krasnopolsky, V. A. (2014). Observations of the CO dayglow at 4.7μm on Mars: Variations of temperature and CO mixing ratio at 50km. *Icarus*, *228*, 189–196. https://doi.org/10.1016/j.icarus.2013.10.008

Krasnopolsky, V. A. (2015). Variations of carbon monoxide in the martian lower atmosphere. *Icarus*, *253*, 149–155. https://doi.org/10.1016/j.icarus.2015.03.006

Krasnopolsky, V. A. (2017). Annual mean mixing ratios of N2, Ar, O2, and CO in the martian atmosphere. *Planetary and Space Science*, *144*, 71–73. https://doi.org/10.1016/j.pss.2017.05.009

Lefèvre, F., & Krasnopolsky, V. (2017). Atmospheric Photochemistry. In R. M. Haberle, R. T. Clancy, F. Forget, M. D. Smith, & R. W. Zurek (Eds.), *The Atmosphere and Climate of Mars* (pp. 405–432). Cambridge University Press.

Lefèvre, F., Lebonnois, S., Montmessin, F., & Forget, F. (2004). Three-dimensional modeling of ozone on Mars. *J. Geophys. Res.*, *109*(E7), E07004. https://doi.org/10.1029/2004JE002268

Lefèvre, F., Trokhimovskiy, A., Fedorova, A., Baggio, L., Lacombe, G., Määttänen, A., et al. (2021). Relationship between the ozone and water vapor columns on Mars as observed by SPICAM and calculated by a global climate model. *Journal of Geophysical Research: Planets*, *126*, e2021JE006838. https://doi.org/10.1029/2021JE006838

Lellouch, E., Encrenaz, T., Phillips, T., Falgarone, E., & Billebaud, F. (1991). Submillimeter observations of CO in Mars' atmosphere. *Planetary and Space Science*, *39*(1), 209–212. https://doi.org/10.1016/0032-0633(91)90143-X

Li, G., Gordon, I.E., Rothman L.S., Tan, Y., Hu, S.-M., Kassi, S., Campargue, A. and Medvedev, E.S. (2015). «ROVIBRATIONAL LINE LISTS FOR NINE ISOTOPOLOGUES OF THE CO MOLECULE IN THE X 1 Σ + GROUND ELECTRONIC STATE». *The Astrophysical Journal Supplement Series* 216 (1): 15. https://doi.org/10.1088/0067-0049/216/1/15.

McElroy, M. B. and Donahue, T.B. (1972). Stability of the Martian Atmosphere. *Science* 177 (4053): 986–88. https://doi.org/10.1126/science.177.4053.986.

Millour E., Francois Forget, Aymeric Spiga, Margaux Vals, Vladimir Zakharov, Luca Montabone, Franck Lefèvre, Franck Montmessin, Jean-Yves Chaufray, Miguel López-Valverde, Francisco González-Galindo, Stephen Lewis, Peter Read, Marie-Christine Desjean, and Fabrice Cipriani The Mars Climate Database (MCD version 5.3), Geophysical Research Abstracts, Vol. 21, EGU2019-7153, 2019, EGU General Assembly 2019

Montabone, L., Spiga, A., Kass, D. M., Kleinböhl, A., Forget, F., & Millour, E. (2020). Martian Year 34 Column Dust Climatology from Mars Climate Sounder Observations: Reconstructed Maps and Model Simulations. *J. Geophys. Res.*

Nair, H., Allen, M., Anbar, A. D., Yung, Y. L., & Clancy, R. T. (1994). A Photochemical Model of the Martian Atmosphere. *Icarus*, *111*(1), 124–150. https://doi.org/10.1006/icar.1994.1137

Olsen, K. S., Lefèvre, F., Montmessin, F., Fedorova, A. A., Trokhimovskiy, A., Baggio, L., et al. (2021). The vertical structure of CO in the Martian atmosphere from the ExoMars Trace Gas Orbiter. *Nature Geoscience*, *14*(2), 67–71. https://doi.org/10.1038/s41561-020-00678-w

Parkinson, T. D., and D. M. Hunten. (1972). Spectroscopy and Aeronomy of O2 on Mars. *Journal of the Atmospheric Sciences* 29 (7): 1380–90. https://doi.org/10.1175/1520-0469(1972)029<1380:saaooo>2.0.co;2.

Shakun, A., Ignatiev, N., Luginin, M., Grigoriev, A., Moshkin, B., Grassi, D., Arnold, G. (2018). ACS/TIRVIM: Calibration and first results, Proc. SPIE 10765, Infrared Remote Sensing and Instrumentation XXVI, 107650E,https://d.docs.live.net/1416dfd2d615e64f/ https://doi.org/10.1117/12.2322163.

Sindoni, G., Formisano, V., & Geminale, A. (2011). Observations of water vapour and carbon monoxide in the Martian atmosphere with the SWC of PFS/MEX. *Planet. Space Sci.*, *59*, 149–162. https://doi.org/10.1016/j.pss.2010.12.006

Smith, M. D. (2019). THEMIS Observations of the 2018 Mars Global Dust Storm. *Journal of*

Geophysical Research: Planets, *124*(11), 2929–2944. https://doi.org/10.1029/2019je006107

Smith, M. D., Daerden, F., Neary, L., & Khayat, A. S. J. (2018). The climatology of carbon monoxide and water vapor on Mars as observed by CRISM and modeled by the GEM-Mars general circulation model. *Icarus*, *301*, 117–131. https://doi.org/10.1016/j.icarus.2017.09.027

Smith, M. D., Daerden, F., Neary, L., Khayat, A. S. J., Holmes, J. A., Patel, M. R., et al. (2021). The climatology of carbon monoxide on Mars as observed by NOMAD nadir-geometry observations. *Icarus*, *362*, 114404. https://doi.org/10.1016/j.icarus.2021.114404

Smith, M. D., Wolff, M. J., Clancy, R. T., & Murchie, S. L. (2009). Compact Reconnaissance Imaging Spectrometer observations of water vapor and carbon monoxide. *J. Geophys. Res.*, *114*, E00D03. https://doi.org/10.1029/2008JE003288

Sprague, A. L., Boynton, W. V., Forget, F., Lian, Y., Richardson, M., Starr, R., et al. (2012). Interannual similarity and variation in seasonal circulation of Mars' atmospheric Ar as seen by the Gamma Ray Spectrometer on Mars Odyssey. *Journal of Geophysical Research: Planets*, *117*(E4). https://doi.org/10.1029/2011JE003873

Sprague, A. L., Boynton, W. V., Kerry, K. E., Janes, D. M., Hunten, D. M., Kim, K. J., et al. (2004). Mars' South Polar Ar Enhancement: A Tracer for South Polar Seasonal Meridional Mixing. *Science*, *306*(5700), 1364–1367. https://doi.org/10.1126/science.1098496

Sprague, A. L., Boynton, W. V., Kerry, K. E., Janes, D. M., Kelly, N. J., Crombie, M. K., et al. (2007). Mars' atmospheric argon: Tracer for understanding Martian atmospheric circulation and dynamics. *Journal of Geophysical Research: Planets*, *112*(E3). https://doi.org/10.1029/2005JE002597

Trainer, M. G., Wong, M. H., McConnochie, T. H., Franz, H. B., Atreya, S. K., Conrad, P. G., et al. (2019). Seasonal Variations in Atmospheric Composition as Measured in Gale Crater, Mars. *Journal of Geophysical Research: Planets*, *124*(11), 3000–3024. https://doi.org/10.1029/2019JE006175

Trokhimovskiy, A., Korablev, O., Kalinnikov, Y. K., Fedorova, A., Stepanov, A. V., Titov, A. Y., et al. (2015a). Near-infrared echelle-AOTF spectrometer ACS-NIR for the ExoMars Trace Gas Orbiter. In *Infrared Remote Sensing and Instrumentation XXIII* (Vol. 9608, pp. 62–70). SPIE. https://doi.org/10.1117/12.2190369

Trokhimovskiy, A., Korablev, O., Ivanov, Y. S., Siniyavsky, I. I., Fedorova, A., Stepanov, A. V., et al. (2015b). Middle-infrared echelle cross-dispersion spectrometer ACS-MIR for the ExoMars Trace Gas Orbiter. In *Infrared Remote Sensing and Instrumentation XXIII* (Vol. 9608, pp. 55–61). SPIE. https://doi.org/10.1117/12.2190359

Trokhimovskiy, A., Perevalov, V., Korablev, O., Fedorova, A. F., Olsen, K. . S., Bertaux, J.-L., et al. (2020). First observation of the magnetic dipole CO_2 main isotopologue absorption band at 3.3 μm in the atmosphere of Mars by ACS. *Astron. Astrophys. in Press*. https://doi.org/10.1051/0004-6361/202038134

Vandaele, A. C., Lopez-Moreno, J.-J., Patel, M. R., Bellucci, G., Daerden, F., Ristic, B., et al. (2018). NOMAD, an Integrated Suite of Three Spectrometers for the ExoMars Trace Gas Mission: Technical Description, Science Objectives and Expected Performance. *Space Sci. Rev.*, *214*, 80. https://doi.org/10.1007/s11214-018-0517-2

Figure 1.

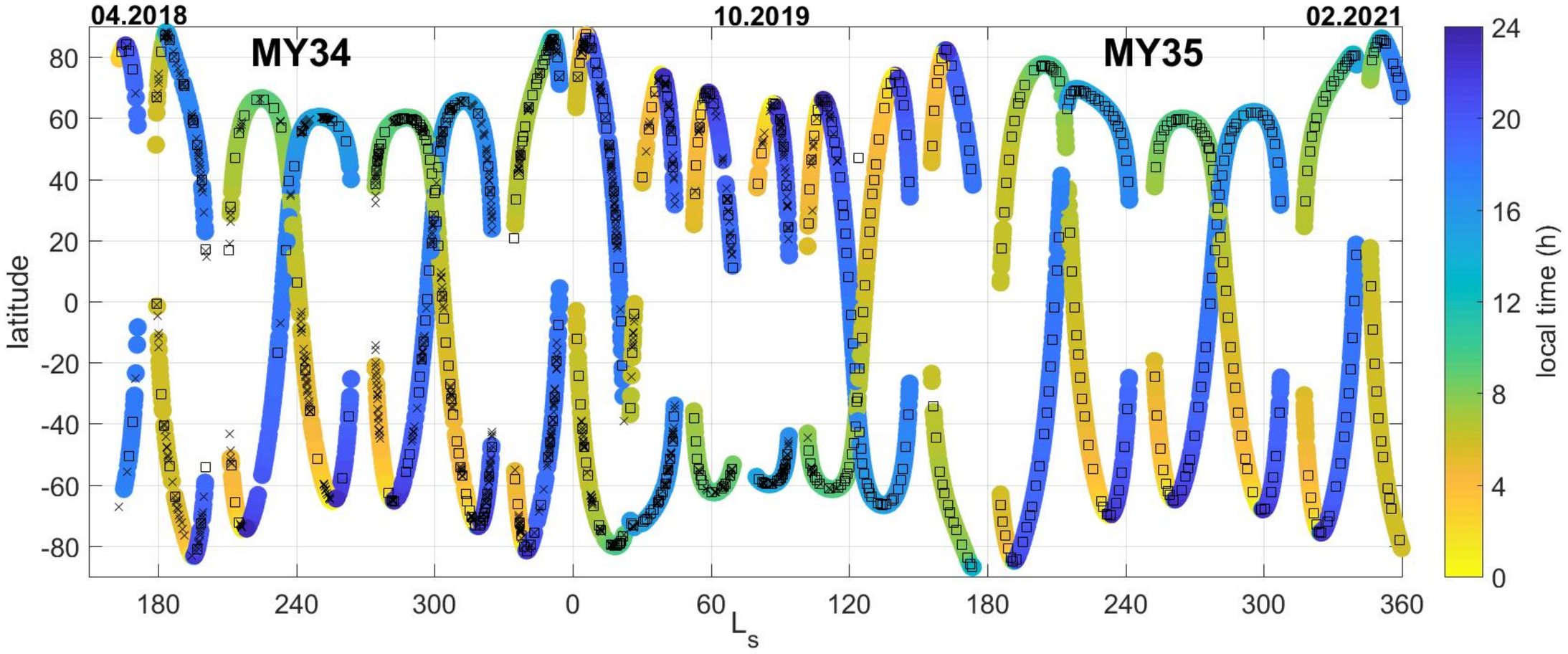
04.2018
10.2019
02.2021
MY34
MY35
latitude
80
60
40
20
0
-20
-40
-60
-80
180
240
300
0
60
120
180
240
300
360
L_s
local time (h)
24
20
16
12
8
4
0

Figure 2.

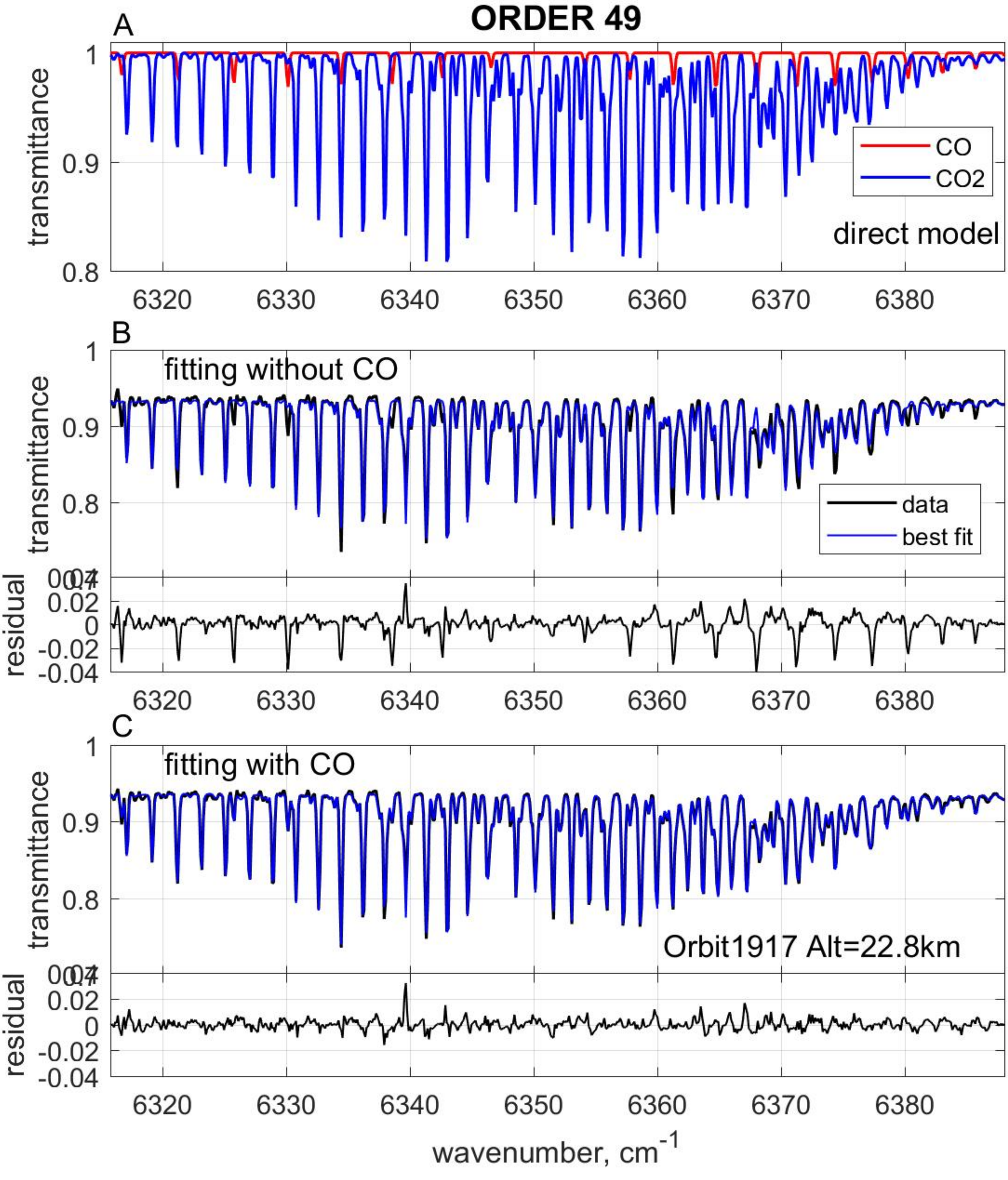
ORDER 49
A
transmittance
1
0.9
0.8
CO
CO2
direct model
6320
6330
6340
6350
6360
6370
6380
B
fitting without CO
transmittance
1
0.9
0.8
data
best fit
residual
0.04
0.02
0
-0.02
-0.04
6320
6330
6340
6350
6360
6370
6380
C
fitting with CO
transmittance
1
0.9
0.8
Orbit1917 Alt=22.8km
residual
0.04
0.02
0
-0.02
-0.04
6320
6330
6340
6350
6360
6370
6380
wavenumber, cm-1

Figure 3.

A

Transmittance

CO
CO_2
H_2O
HDO

245
246
247
248
249

B

MIR
the best fit

ORDER 249 orbit1853 Alt=24km

C

Residual

Wavenumber, cm^{-1}

Figure 4.

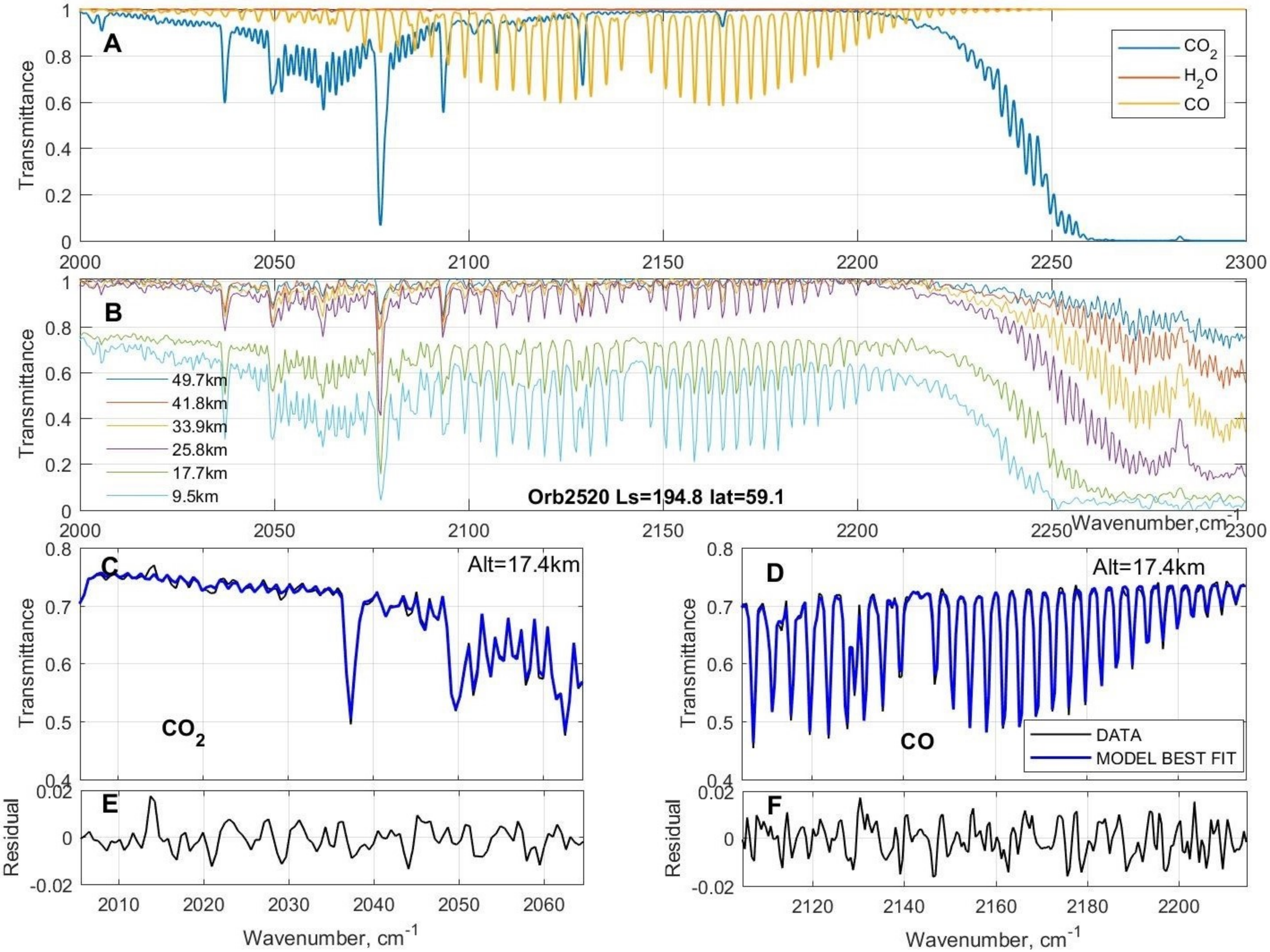
A
Transmittance
CO_2
H_2O
CO
B
49.7km
41.8km
33.9km
25.8km
17.7km
9.5km
Orb2520 Ls=194.8 lat=59.1
Wavenumber,cm^{-1}
C
Alt=17.4km
CO_2
D
CO
DATA
MODEL BEST FIT
E
F
Residual
Wavenumber, cm^{-1}

Figure 5.

Orbit2266 Ls=182.84 Lat=86.98

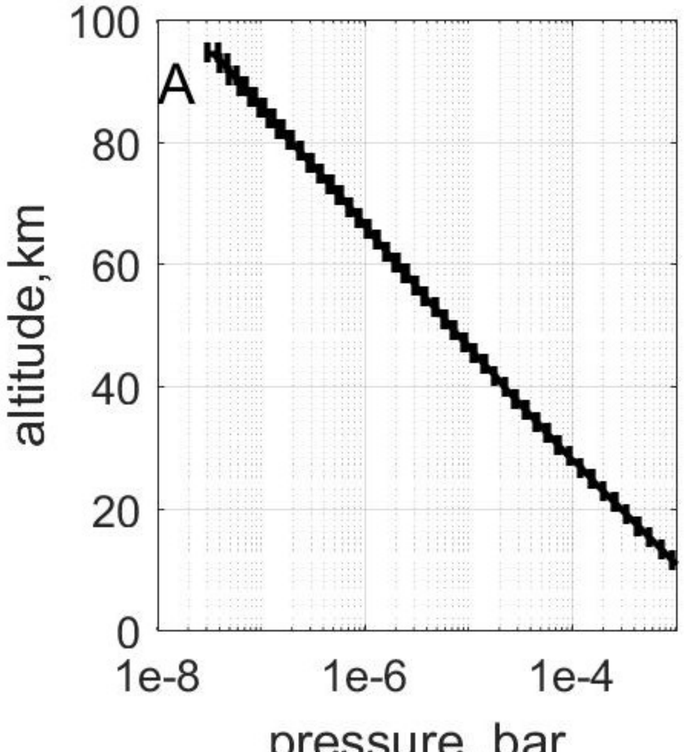

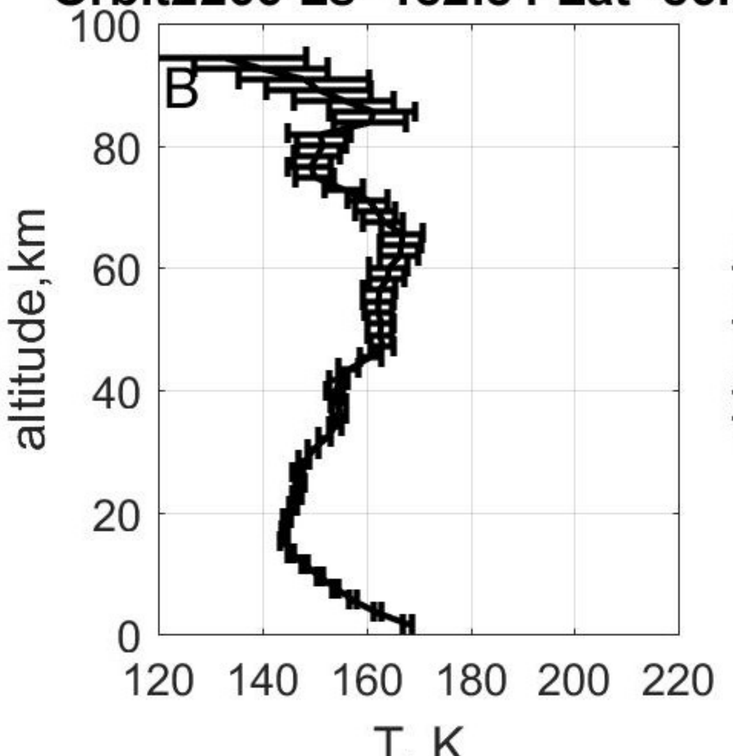

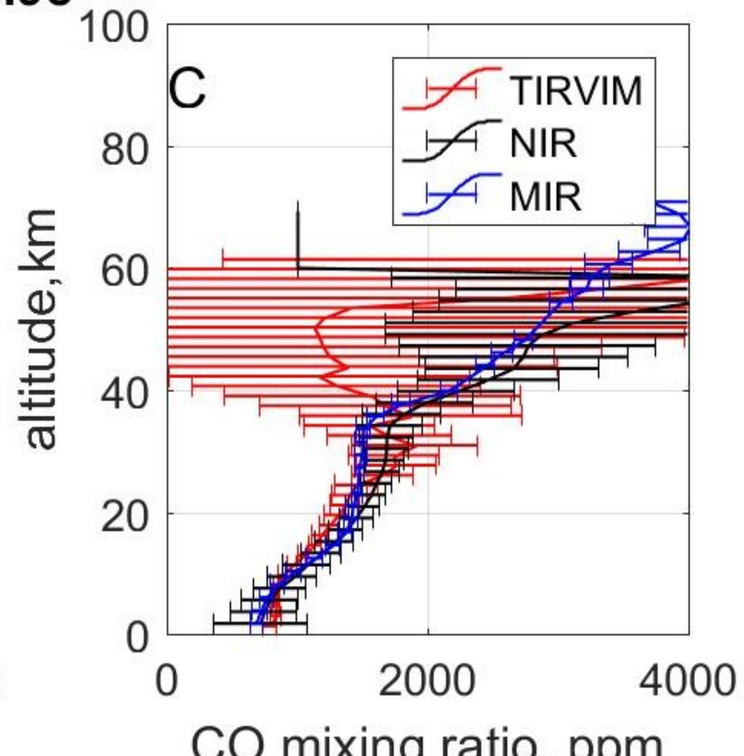

Orbit4229 Ls=281.83 Lat=-65.03

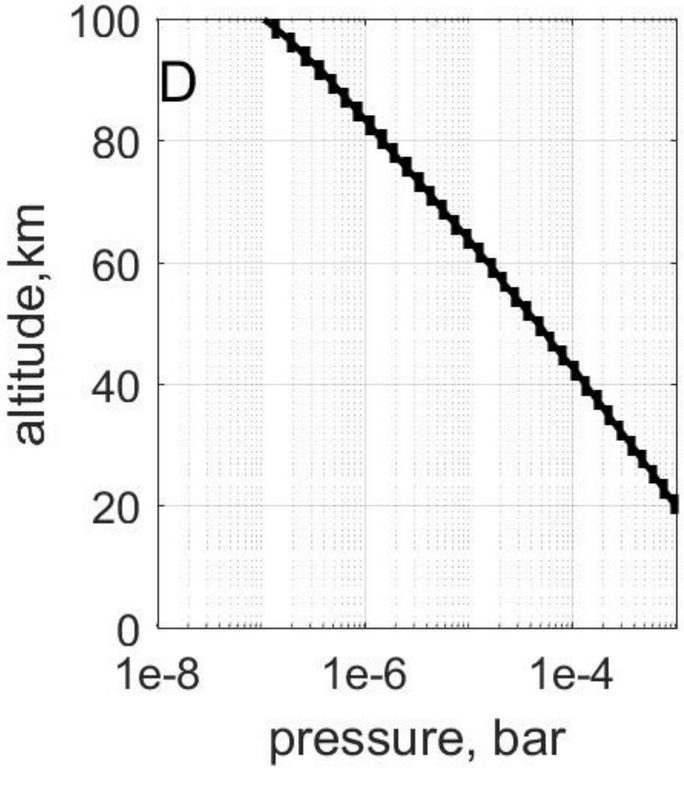

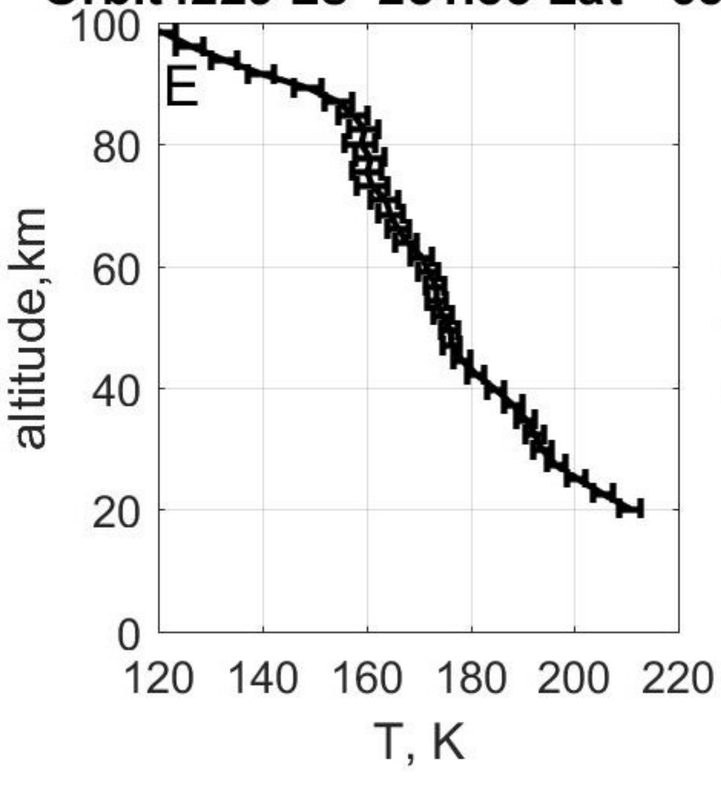

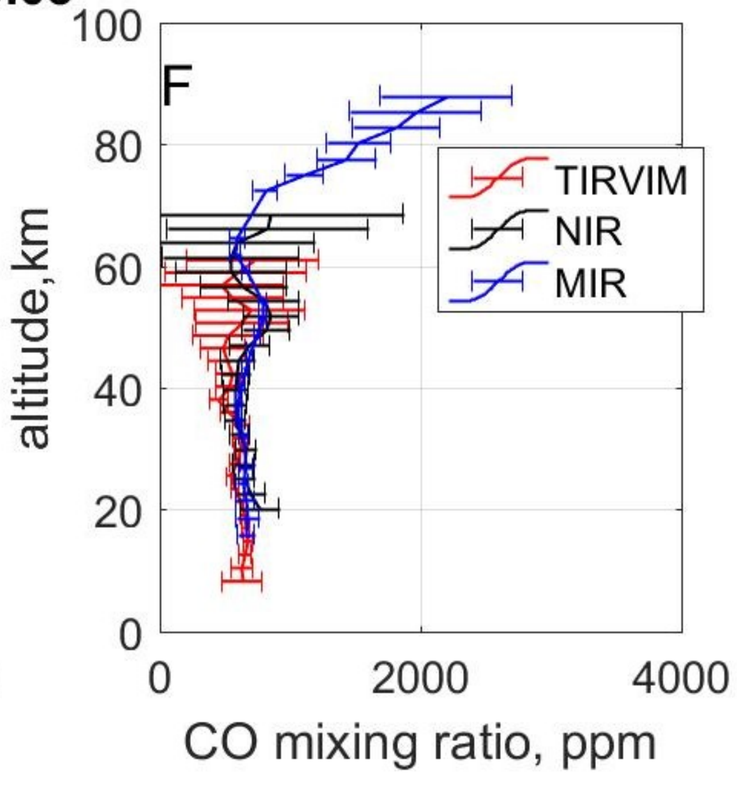

Figure 6.

Minimal sounded altitude, km

A

latitude

80 60 40 20 0 -20 -40 -60 -80

180 240 300 0 60 120 180 240 300 360

50 40 30 20 10 0

CO mixing ratio (ppmv) at 20 km

B

MY34

MY35

2400 2000 1600 1200 800 400

CO mixing ratio (ppmv) at 40 km

C

L_s

2400 2000 1600 1200 800 400

CO(40km) - CO(20km), percent

C

L_s

100 60 20 -20 -60 -100

Figure 7.

NIR CO, ppm

MIR CO, ppm

GCM CO, ppm

MY34

MY35

Ls 150-180°
Ls 180-210°
Ls 210-240°
Ls 240-270°
Ls 270-300°
Ls 300-330°
Ls 330-360°
Ls 0-30°
Ls 30-60°
Ls 60-90°
Ls 90-120°
Ls 120-150°
Ls 150-180°
Ls 180-210°
Ls 210-240°
Ls 240-270°
Ls 270-300°
Ls 300-330°
Ls 330-360°

z, km

0
50

-90 -60 -30 0 30 60 90

latitude

3000
2800
2600
2400
2200
2000
1800
1600
1400
1200
1000
800
600
400

Figure 8.

A

MY34

MY35

CO mixing ratio, ppmv

1600
1400
1200
1000
800
600
400

180 240 300 0 60 120 180 240 300 360

CO NIR
CO MIR pos6
CO MIR, Olsen et al., 2021
TIR
GCM

PFS,Bouche et al., 2021

B

MY34

MY35

CO mixing ratio, ppmv

1600
1400
1200
1000
800
600
400

180 240 300 0 60 120 180 240 300 360

L_s

CRISM
NOMAD
NIR averaged
MIR averaged
TIR averaged

Figure 9.

MY34

MY35

latitude

Ls

altitude, km

ACS-NIR

LMD GCM

NIR T

GCM T

CO, ppmv

T, K

Figure 10.

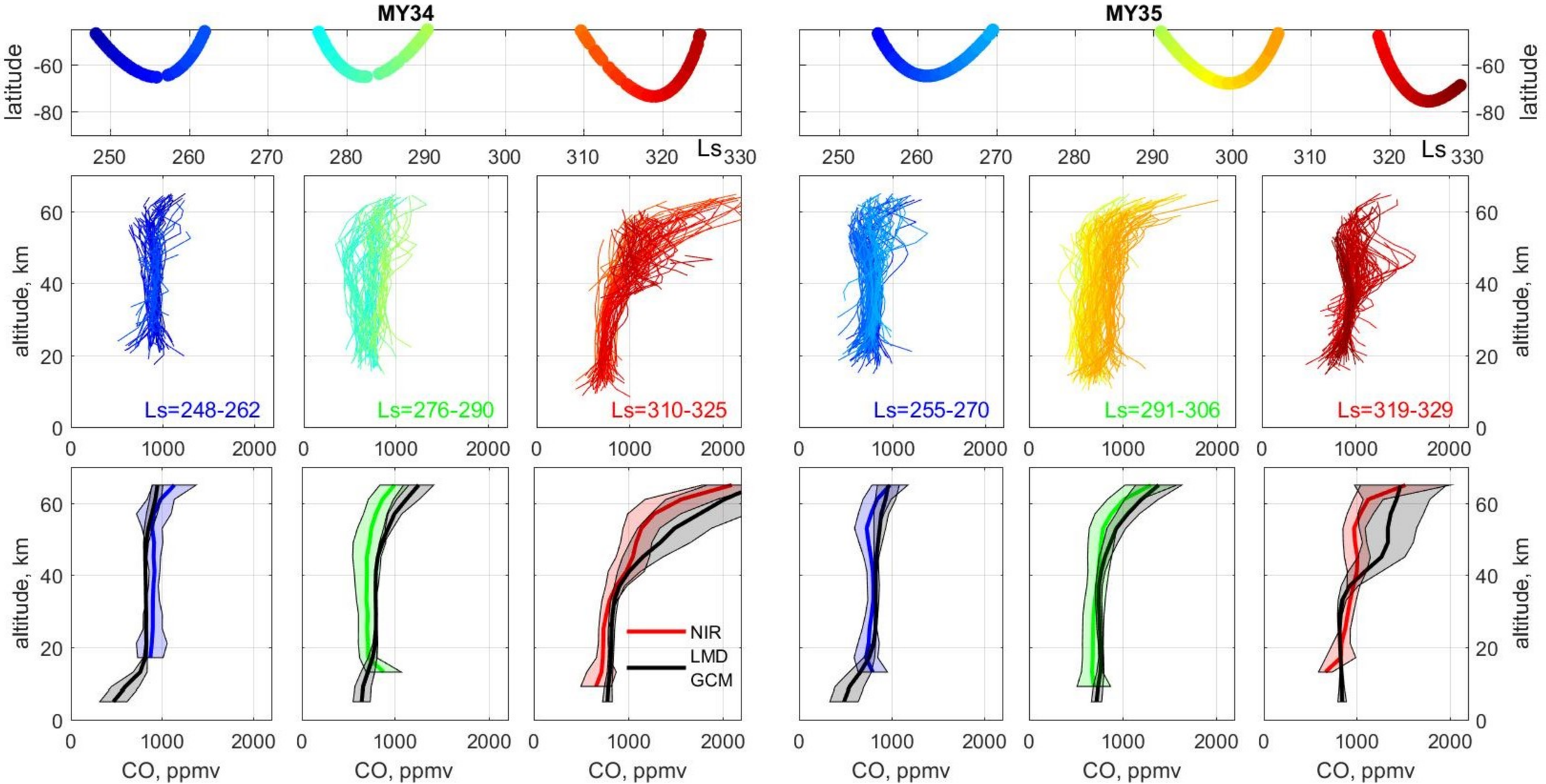
MY34
MY35
latitude
-60
-80
250
260
270
280
290
300
310
320
Ls
330
altitude, km
0
20
40
60
0
1000
2000
Ls=248-262
Ls=276-290
Ls=310-325
Ls=255-270
Ls=291-306
Ls=319-329
NIR
LMD
GCM
CO, ppmv

Figure 11.

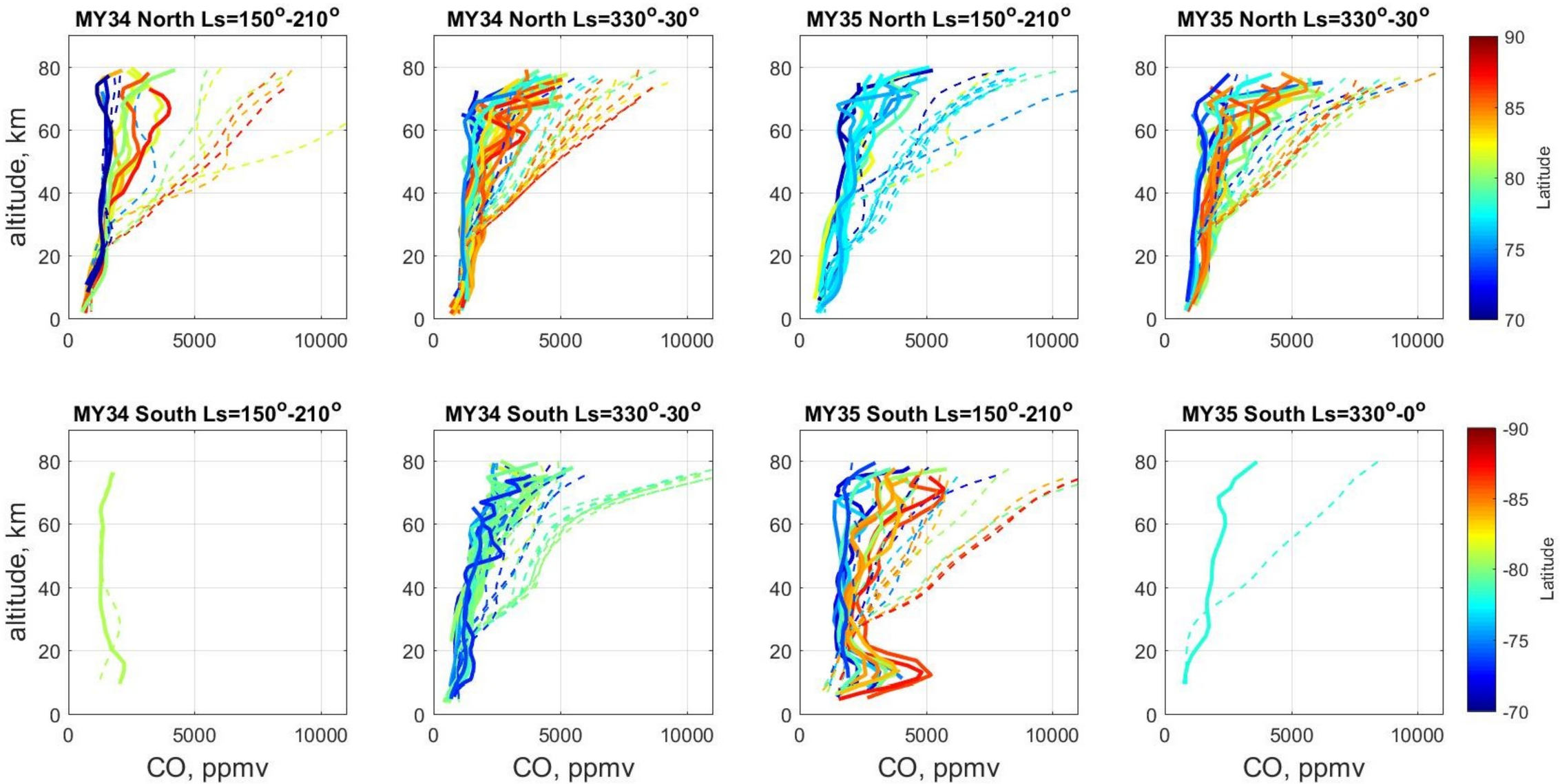
MY34 North Ls=150°-210°
MY34 North Ls=330°-30°
MY35 North Ls=150°-210°
MY35 North Ls=330°-30°
MY34 South Ls=150°-210°
MY34 South Ls=330°-30°
MY35 South Ls=150°-210°
MY35 South Ls=330°-0°
altitude, km
CO, ppmv
0
20
40
60
80
0
5000
10000
Latitude
90
85
80
75
70
-90
-85
-80
-75
-70

Figure 12.

MY34
MY35
Ls
180
190
200
210
220
230
240
latitude
50
0
-50
MY34 Ls 180-190
MY35 Ls 180-190
MY35-MY34 Ls 180-190
MY34 Ls 190-200
MY35 Ls 190-200
MY35-MY34 Ls 190-200
MY34 Ls 200-210
MY35 Ls 200-210
MY35-MY34 Ls 200-210
MY34 Ls 210-220
MY35 Ls 210-220
MY35-MY34 Ls 210-220
MY34 Ls 220-230
MY35 Ls 220-230
MY35-MY34 Ls 220-230
MY34 Ls 230-240
MY35 Ls 230-240
MY35-MY34 Ls 230-240
altitude, km
0
20
40
60
80
latitude
-90
-60
-30
0
30
60
90
CO, ppm
3000
2500
2000
1500
1000
500
CO_{MY35}-CO_{MY34}, percents
40
30
20
10
0
-10
-20
-30
-40